University of Alberta

Electromechanical Behaviour of Surface-Bonded Piezoelectric Sensors/Actuators with Imperfect Adhesive Layers

by

Congrui Jin

A thesis submitted to the Faculty of Graduate Studies and Research
in partial fulfillment of the requirements for the degree of

Master of Science

Department of Mechanical Engineering

Fall 2009
Edmonton, Alberta

Examining Committee

Xiaodong Wang, Mechanical Engineering, University of Alberta

Mingjian Zuo, Mechanical Engineering, University of Alberta

Peter Schiavone, Mechanical Engineering, University of Alberta

Dongyang Li, Chemical Engineering, University of Alberta

Abstract

The performance of smart structures depends on the electromechanical behaviour of piezoelectric sensors/actuators and the bonding condition along the interface, which connects the sensor/actuator and the host structures. This thesis documents a theoretical study of the influence of material parameters of the imperfect bonding layer on the coupled electromechanical characteristics of piezoelectric sensors/actuators. A one dimensional sensor/actuator model with an imperfect bonding layer, which undergoes a shear deformation, is proposed. The emphasis of the current study is on the local stress and strain fields near imperfectly bonded sensors/actuators and the load transfer. Analytical solutions based on the integral equation method are provided. Detailed numerical simulation is conducted to evaluate the influence of the geometry and the material mismatch of the adhesive layer upon the sensing/actuating process. The interfacial debonding and its effect upon the strain/stress distribution and the overall performance of the integrated structure are evaluated in detail.

Acknowledgements

I thank my thesis advisor, Dr. Xiaodong Wang, for his constant assistance, encouragement, guidance and the tremendous support and opportunities he provided throughout my master studies at University of Alberta. He taught me how to undertake research, and helped sharpen my thinking. This experience has been, and will continue to be, invaluable to me.

I thank my thesis co-advisor, Dr. Mingjian Zuo, for his continuous encouragement, optimism and confidence in me. Without his guidance and support this research would not have been possible. I am indebted to him for the time and energy he spent on my research.

I thank Professors Peter Schiavone and Dongyang Li for their guidance, encouragement and insightful advice while serving as my thesis committee members.

Contents

1 Introduction **1**

1.1 Background 1

1.2 Research Objectives 3

1.3 Organization of the Thesis 4

2 Literature Review **5**

2.1 History of Piezoelectricity and Piezoelectric Ceramics 5

2.2 Global Response of the Piezoelectric System 7

2.3 Electromechanical (E/M) Impedance Technique 8

2.4 Elastic Wave Propagation in Piezoelectric System 9

2.5 Studies on the Effect of the Bonding Layers 11

3 Analysis of the Piezoelectric Actuator System **13**

3.1 Introduction 13

3.2 Formulation of the Problem 14

3.2.1 The actuator 14

3.2.2 The bonding layer 17

3.2.3 The host medium 17

3.2.4 Static load transfer in a perfectly bonded piezoelectric actuator 18

3.2.5 Effect of interfacial debonding 20
3.3 Numerical Results and Discussion 29
3.3.1 Actuator with a uniform interfacial layer 30
3.3.2 Interfacial debonding 33
3.4 Concluding Remarks 44

4 Analysis of the Piezoelectric Sensor System 45
4.1 Introduction 45
4.2 Formulation of the Problem 46
4.2.1 The sensor 46
4.2.2 The bonding layer 47
4.2.3 The host medium 48
4.2.4 Static load transfer in a perfectly bonded piezoelectric sensor 49
4.2.5 Effect of interfacial debonding 50
4.3 Numerical Results and Discussion 55
4.3.1 Sensor with a uniform interfacial layer 56
4.3.2 Interfacial debonding 61
4.4 Concluding Remarks 71

5 Final Remarks 72
5.1 Contributions and Conclusions 72
5.2 Future Work 74

Bibliography 76

List of Tables

3.1 Material Properties of the Piezoelectric Actuator 31
3.2 Material Properties of the Host Medium and the Bonding Layer 31

4.1 Material Properties of the Host Medium and the Bonding Layer 56

List of Figures

3.1 Schematics of the actuator configuration. 15

3.2 Schematics of edge debonding. 22

3.3 Schematics of interior debonding. 24

3.4 Interfacial shear stress distribution ($q = 2.28$, $v = 0.2$ and $v' = 0$). Solutions obtained from current model are shown as lines and FEA as data points. 36

3.5 Interfacial shear stress distribution ($q = 1.0$ and $v' = 0$). 36

3.6 Interfacial shear stress distribution ($q = 1.0$, $q' = 0.011$ and $v' = 0.01$). 37

3.7 Interfacial shear stress distribution ($v = 0.05$ and $v' = 0$). . . . 37

3.8 Interfacial shear stress distribution ($q' = 0.011$, $v = 0.05$ and $v' = 0.01$). 38

3.9 Interfacial shear stress distribution ($q = 1.0$, $q' = 0.011$ and $v = 0.05$). 38

3.10 $\tau^*(\eta_e)$ as a function of d/a ($q = 1.0$, $q' = 0.011$ and $v = 0.05$). . 39

3.11 Interfacial shear stress distribution ($q = 1.0$, $v = 0.05$ and $v' = 0$). 39

3.12 Interfacial shear stress distribution ($q = 1.0$, $q' = 0.011$, $v = 0.05$ and $v' = 0.01$). 40

3.13 Interfacial shear stress distribution ($q = 1.0$, $d/a = 0.6$ and $v' = 0$). 40

3.14 Interfacial shear stress distribution ($q = 1.0$, $q' = 0.011$, $d/a = 0.6$ and $v' = 0.01$). 41
3.15 Interfacial shear stress distribution ($q = 1.0$, $q' = 0.011$, $v = 0.05$ and $d/a = 0.6$). 41
3.16 $\tau^*(\eta_{el})$ as a function of d/a ($q = 1.0$, $q' = 0.011$ and $v = 0.05$). . 42
3.17 $\tau^*(\eta_{er})$ as a function of d/a ($q = 1.0$, $q' = 0.011$ and $v = 0.05$). . 42
3.18 σ^* as a function of d/a ($q = 1.0$, $q' = 0.011$ and $v = 0.05$). 43

4.1 Amplitude of strain ratio ($q = 0.3928$ and $v' = 0$). Solutions obtained from current model are shown as lines and FEA as data points. 63
4.2 Amplitude of strain ratio ($q = 0.3928$, $q' = 0.0083$ and $v' = 0.015$). 64
4.3 Amplitude of strain ratio ($v = 0.05$ and $v' = 0$). 64
4.4 Amplitude of strain ratio ($v = 0.05$, $q' = 0.0083$ and $v' = 0.01$). . 65
4.5 Amplitude of strain ratio ($q = 0.3928$, $q' = 0.0083$ and $v = 0.05$). 65
4.6 Amplitude of strain ratio ($q = 10.0$, $q' = 0.0083$ and $v = 0.05$). 66
4.7 Normalized voltage distribution with different thicknesses of the bonding layer and material combinations ($q' = 0.0083$ and $v = 0.05$). 66
4.8 Normalized voltage distribution with different thicknesses of the bonding layer and sensor geometries ($q = 0.3928$ and $q' = 0.0083$). 67
4.9 Normalized output voltage as a function of debonding length ($q = 0.3928$, $q' = 0.0083$ and $v = 0.05$). 67
4.10 Amplitude of strain ratio ($q = 2.0$, $v = 0.05$ and $v' = 0$). 68
4.11 Amplitude of strain ratio ($q = 2.0$, $v = 0.05$, $q' = 0.0083$ and $v' = 0.01$). 68

4.12 Amplitude of strain ratio ($v = 0.05$ and $v' = 0$). Red lines: undebonded cases ($d/a = 0$). Blue lines: debonded cases ($d/a = 0.6$). 69
4.13 Amplitude of strain ratio ($v = 0.05$, $q' = 0.0083$ and $v' = 0.01$). Red lines: undebonded cases ($d/a = 0$). Blue lines: debonded cases ($d/a = 0.6$) 69
4.14 Amplitude of strain ratio ($q = 10.0$, $q' = 0.0083$ and $v = 0.05$). Red lines: undebonded cases ($d/a = 0$). Blue lines: debonded cases ($d/a = 0.6$). 70
4.15 Normalized output voltage as a function of debonding length ($q = 0.3928$, $q' = 0.0083$ and $v = 0.05$). 70

Chapter 1

Introduction

1.1 Background

The piezoelectric materials have been a primary focus of attention in the research of smart materials and structural systems because of their ability to transform electrical energy to mechanical energy, and vice versa, i.e., to function both as actuators and sensors [1–4]. Optimizing the effectiveness and reliability of integrated sensor/actuator systems requires a clear understanding of the sensing/actuating processes and the resulting electromechanical response of the whole structure. In addition, the bonding condition between the sensor/actuator and the host structure will also affect the performance of the sensor/actuator [5–8]. It becomes, therefore, an important issue to study the coupled electromechanical behaviour of these sensors/actuators with bonding layers to reliably evaluate the relation between the measured signal and the local mechanical deformation.

Due to the presence of material discontinuity between the piezoelectric sensors/actuators and the host structure, complicated local electromechanical fields will be generated near the edge of sensors/actuators, which will affect the load transfer between the sensor/actuator and the host structure, and there-

fore influence the performance of the sensor/actuator. To study the static load transfer between the piezoelectric elements and the host structure, simplified sensor/actuator models have been established. A beam-like structure with surface-bonded and embedded thin-sheet piezoelectric elements is first analyzed to study the load transfer [9]. In this analysis, the axial stress in the piezoelectric elements is assumed to be uniform across their thickness. A Bernoulli–Euler model of a piezoelectric thin-sheet bonded to a beam is further developed by considering the linear stress distribution across the thickness of the piezoelectric element [10]. A refined sensor model based on the plane stress condition was presented for a beam structure with symmetrically surface-bonded sensor patches [11, 12]. Plate and shell models have also been extensively used in modelling the electromechanical behaviour of piezoelectric structures [13–19]. The static local stress field near a thin-sheet piezoelectric element attached to an infinite elastic medium is studied to investigate the stress concentration and the load transfer between the piezoelectric element and the host medium [20]. Similar analysis is also conducted to determine the static electromechanical field of a piezoelectric layer bonded to an elastic medium with both interfacial and normal stresses being considered [21, 22].

Significant attention has also been paid to the modelling of debonding of sensors/actuators. Ref. [23] investigated the effects of debonding between piezoelectric sensors/actuators on the behaviour of smart composite plates by using an FE model based on the "free mode" assumption. Continuity conditions at the delamination junctions were satisfied using the penalty function approach. The results of the numerical model were in good agreement with the experimental data [24]. Refs. [25–27] presented analytical models for a smart beam with a debonded piezoelectric sensor/actuator. It was assumed

that there is no stress transfer between the host beam and the piezoelectric sensor/actuator in the debonding region. Using similar assumptions Ref. [28] presented a finite element model based on the first-order shear deformation theory. A closed-loop-control-based damage detection scheme is presented by Ref. [29] aiming at detecting damage in structures. The results show that even a small edge debonding in a piezoelectric sensor patch can make the sensitive control system unstable, and therefore can be detected. Ref. [30] investigated the effect of the shear lag loss on electromechanical impedance measurements, and found that the bonding layer can significantly modify the measured admittance signatures. A useful review is given by Ref. [31].

1.2 Research Objectives

The objective of this thesis is to study of effects of the imperfect bonding layer on the load transfer between a surface-bonded piezoelectric sensor/actuator and the elastic host medium. The current work is an extension of the work presented in Refs. [85, 86] in which an integrated model containing a piezoelectric thin-sheet sensor/actuator, a viscoelastic bonding layer and an elastic medium (host) is proposed to evaluate its dynamic property under different loading frequencies. Although the effect of the geometrical and material property of the system has been investigated intensively, less effort has been devoted to the study of the debonding. In this thesis, we focus on the effect of interfacial debonding in the static case where the loading frequency is so low that the typical wavelength of the incident wave is much longer than the length of the sensor/actuator. The imperfect bonding and its effect upon the strain/stress distribution and the overall performance of the structure are evaluated in detail. Numerical simulation is conducted to simulate the effect of

the geometrical and material property of the system, especially that of the imperfect bonding layer upon the coupled response of the sensors/actuators.

1.3 Organization of the Thesis

The thesis is organized as follows. The current progress and relevant theories and techniques needed in modelling the sensor/actuator system are reviewed in Chapter 2. A one dimensional actuator model is established in Chapter 3, and the effects of the bonding layer properties on the static electromechanical behavior of the actuator system are discussed. A modified sensor model is established in Chapter 4, and the effects of the bonding layer properties on the static behaviour of the sensor system are studied. Finally, the conclusions and contributions of this thesis are summarized in Chapter 5, and perspective topics are suggested for future studies.

Chapter 2

Literature Review

2.1 History of Piezoelectricity and Piezoelectric Ceramics

Piezoelectricity is the ability of materials to generate surface charges in response to applied mechanical strain. The piezoelectric effect was discovered in the late 19th century by Pierre and Jacques Curie. They combined their knowledge of pyroelectricity with their understanding of the underlying crystal structures that gave rise to pyroelectricity to predict crystal behavior, and demonstrated the effect using crystals of tourmaline, quartz, topaz, cane sugar, and Rochelle salt. Quartz and Rochelle salt exhibited the most piezoelectricity. The Curies, however, did not predict the converse piezoelectric effect. The converse effect was mathematically deduced from fundamental thermodynamic principles by Gabriel Lippmann in 1881. The Curies immediately confirmed the existence of the converse effect, and went on to obtain quantitative proof of the complete reversibility of electro-elasto-mechanical deformations in piezoelectric crystals.

Early applications harnessed the ability of piezoelectric devices to act as transducers between electric potential and frequency. The first practical application of piezoelectric devices was the development of sonar during World

War I. Langevin produced a transducer composed of thin quartz crystals sandwiched between steel plates. Ultrasound was generated by the piezoelectric device and subsequently detected by an underwater microphone. Based on the time for the ultrasonic pulse to be detected, spatial distances could accurately be determined.

During World War II, independent research groups in the United States, Russia, and Japan discovered a new class of man-made materials, called ferroelectrics, which exhibited piezoelectric constants many times higher than natural materials. This led to intense research to develop barium titanate and later lead zirconate titanate materials with specific properties for particular applications [32–35]. Compared with natural piezoelectric crystals, these newly discovered and developed piezoelectric ceramics are more versatile with physical, chemical and piezoelectric characteristics, and can be tailored for specific applications.

The use of piezoelectric ceramic materials as sensors and actuators in Structural Health Monitoring, Intelligent Structures, etc., has been considerably increased during the past few decades [36–41]. Typically, piezoceramics are used as actuators and polymer piezo films are used as sensing materials. It is also possible to use piezoceramics for both sensing and actuation, as in the case of self-sensing actuators [42]. In addition to the possibility of performing collocated control, such sensors/actuators have other advantages such as compactness, sensitivity over a large strain bandwidth and ease of embeddability for performing structural health monitoring as well as distributed active control functions concurrently.

2.2 Global Response of the Piezoelectric System

As a result of the extensive use of piezoelectric patches in SHM systems, significant attentions have been paid to the studies of the global response of piezoelectric systems [43–51]. In the above studies, issues involving dynamic stability were considered in Refs. [43, 44]. Buckling of beams with piezoelectric actuators was studied in Refs. [45–49]. Control of the vibrations of a beam under axial load was studied in Ref. [50] using a closed-loop control where the sensing was implemented by using the tip deflection of the beam. In Ref. [51] the actuator was taken as the full length of the beam as opposed to a patch one. The solutions of the governing equations in the above studies were achieved either by finite elements or by Fourier series approximations. A simply-supported beam model with a pair of out-of-phase surface-bonded piezoelectric actuators is established to study the beam response when it is excited in bending by the actuators at resonance frequencies [52]. The coupling between the bending, axial and torsional vibrations of composite beams with surface-bonded piezoelectric sensor layers has been studied theoretically [53]. In this study, the ICL composite-beam model is obtained by integrating the existing ICL composite-plate model proposed by Ref. [54]. When the plate width is much smaller than the plate length, integration of the ICL composite-plate equations and linearization of displacement fields lead to a set of equations that couple bending, torsional, and axial vibrations of a composite beam. The equations of motion and associated boundary conditions are normalized and rearranged in a state-space matrix form, and the vibration response is predicted through the transfer function approach developed by Ref. [55].

The use of piezoelectric patches in structural shape control has also been investigated by many researchers. The study of ascertaining the input voltages

for piezoelectric actuators used in the shape control of structural elements was first reported by Refs. [56, 57]. They carried out the bending analysis of composite beams, plates and shells using the Rayleigh–Ritz method. Ref. [58] developed a finite element model for beams with piezoelectric actuators. Ref. [59] proposed a mathematical framework for the deformation of a flexible beam to a desired shape using piezoceramic patch control. Ref. [60] reported experimental results for a Euler–Bernoulli cantilever beam and used these results to verify the analytical results. Ref. [61] developed an exact solution for the static shape control of smart structures by piezoelectric actuation. Analytical solutions for the optimal voltages were developed by Ref. [62] for the shape control of composite laminated cantilever beams based on the first-order shear deformation beam theory. In Ref. [63], the shape control of beams with piezoelectric actuators defined by coupled nonlinear material constitutive equations is investigated. This investigation focuses on the nonlinearity of the material and its effect on the optimal voltages for the shape control problem. To incorporate a nonlinear material behavior in the shape control problem, an iterative finite element model is developed.

2.3 Electromechanical (E/M) Impedance Technique

Electromechanical impedance approach is suitable for near field structural damage detection. The mechanism of the method is to employ structural excitations through surface-bonded piezoelectric patches and to monitor the changes in the impedance of the structure. In the last ten years, extensive effects have been made to promote the development of this technique.

E/M impedance method was pioneered by Refs. [64, 65]. Subsequently, several authors used the E/M impedance method for structural health moni-

toring, by comparing the impedance frequency spectra of various pristine and damaged structures [66, 67]. The method has been shown to be especially effective at ultrasonic frequencies, which properly capture the changes in local dynamics due to incipient structural damage. Such changes are too small to affect the global dynamics and hence cannot be readily detected by conventional low-frequency vibration methods. The method is direct and easy to implement, the only required equipment being an electrical impedance analyzer. The name Electromechanical (E/M) Impedance Method was first used by [68]. Novel ways to interpret the E/M impedance spectra and identify structural damage have been explored by Refs. [69, 70].

Ref. [41] presented a step-by-step derivation of the interaction between the piezoelectric active sensor and the host structure, and produced, for the first time, analytical expressions and numerical results for the E/M admittance and impedance seen at sensor terminal. These numerical results were then directly compared with those experimentally measured at the piezoelectric active sensor terminals during the structural identification process. In their derivation, the limitations of the quasi-static sensor approximation adopted by previous investigators were lifted. Exact analytical expressions were used for structural modeling of simultaneous axial and flexural vibrations.

2.4 Elastic Wave Propagation in Piezoelectric System

The use of piezoelectric patches for damage detection of structures based on elastic wave propagation has attracted significant attention [71–73]. Elastic waves are sensitive to the changes of geometry and parameters of the material, and can propagate over a long distance in a structure. Therefore, they are attractive for the quick, large range inspection of structures. They also have

the potential to detect both surface cracks and embedded damage. Due to these advantages, comparing with other methods for damage detection, such as using electromagnetic field and thermal field [74], elastic waves have been more widely used in active SHM system [75].

The study in Ref. [76] has shown that the E/M impedance method and the wave propagation approach are complementary techniques that should be simultaneously used for damage detection. Since the former method works in the near field, while the latter acts in the far field, their simultaneous utilization will ensure the complete coverage of the monitored structure. In the damage detection process, the signal processing methods and damage-metric algorithms have to be tuned to the specific structural interrogation techniques being used. In the high-frequency E/M impedance approach, pattern recognition methods should be used to compare the impedance signatures and to identify change in these signatures that are indicative of damage presence and progression. In the wave propagation approach, the pulse-echo and acousto-ultrasonic methods identifying the reflections generated from the damage site, and changes in wave phase and velocity, can be used.

However, the major difficulties of using elastic waves to conduct structural health monitoring are that the signals are not instinctually interpretable due to the complicated behaviour of elastic waves, such as the dispersive characteristics of the waves, the presence of multi-modes, and the existence of complicated mode conversions [77]. These difficulties lead to further studies about the interaction between host structures and incorporated piezoelectric sensors/actuators, and the resulting complicated electromechanical behaviour in a smart SHM system [78].

2.5 Studies on the Effect of the Bonding Layers

Recently, several studies have reported that the controllability of smart structures can suffer when the mechanical properties of the bonding layer are ignored in the dynamic model of smart structures [79, 80]. This means, a more complete control model can be obtained if the mechanical properties of the bonding layer have been considered. In Ref. [7], the vibration properties of composite beams with attached sensors and actuators are investigated for three different adhesives. The results of the experimental study reveal that significant differences in the elastic properties of the investigated adhesive materials have only a minor influence on the natural frequencies, damping ratios, and decay times. The experimental study also reveals some localized failure modes due to interfacial debonding.

To show the influence of bonding layer parameters (elastic shear modulus and retardation time) on the dynamic response of the controlled beam, the developed bending-extensional model of a visco-elastic beam with a collocated sensor/actuator system is proposed in Ref. [81]. Taking into account a pure extension in piezoelements, the shear bonding layers both for the actuator and the sensor are assumed as visco-elastic and described by the Kelvin–Voigt material. The results in terms of frequency response of the beam transverse displacements show that the stiffness of bonding layers affects significantly the active damping efficiency. The beam vibrations can be reduced considerably for relatively stiff glue layers.

In Ref. [8], the influence of the compliant adhesive layers on the static response of unidirectional active panels is investigated. Emphasis is put on the effect of the mechanical and geometrical properties of the adhesive layer on the response of the layered structure and on the interlaminar strain and

stress transfer mechanisms. The model derived follows the concepts of the high-order theory developed by Refs. [82, 83]. The results reveal the high-order effects and the stress concentrations in the transition zone near the edge of the panel and indicate that a careful selection of the adhesives properties can improve the behavior of the structure and reduce the severity of the stress concentrations involved.

Ref. [84] addresses the assessment of the quality of the bonding layer of piezoelectric sensors that are mounted on external surfaces of the main structure. Both the external surface and the piezoelectric patches are assumed to be perfectly plane and parallel, having a layer of adhesive joining them together. The equations governing the mechanical equilibrium are simplified by assuming a pure shear stress state in the bonding film. This investigation addresses shear lag effects and shows that end-bonding must be carefully assessed in order to enhance the quality of the sensing output.

Ref. [85] studied the effect of the material and geometric properties of the sensor and the bonding layer on the load transfer from the host medium to the sensor. The results indicate that, for relatively low frequency cases, with the increase of the bonding layer stiffness, the amplitude of the strain distribution along the sensor increases; for very high frequency cases, the strain distribution along the sensor becomes very complicated and unpredictable with the decrease of the bonding layer stiffness. The effect of the bonding condition on the dynamic behavior of the actuators in high frequency cases has been studied [86]. The results indicate that the properties of the bonding layer, the loading frequency, the geometry and material combination of the actuator have a significant effect on the load transfer between the actuator and the host medium.

Chapter 3

Analysis of the Piezoelectric Actuator System

3.1 Introduction

The objective of this chapter is to develop an analytical model to study the coupled electromechanical behaviour of a thin-sheet piezoceramic actuator imperfectly bonded to an elastic half plane under in-plane mechanical and electrical loadings. The current work is an extension of the work presented in Ref. [20] in which the actuator is characterized by an electroelastic line model with the poling direction being perpendicular to its length. An imperfect adhesive bonding layer between the actuator and the host structure is introduced to study the influence of the mechanical and geometrical properties of the adhesive layer on the coupled electromechanical behaviour of the integrated structure. The emphasis of the current study is on the local stress and strain fields near imperfectly bonded actuators and the load transfer. Numerical simulation is conducted to study the influence of the geometry and the material mismatch of the adhesive layer upon the actuation process. The interfacial debonding and its effect upon the stress distribution and the overall performance of the

structure are evaluated in detail.

3.2 Formulation of the Problem

Let us now consider the plane strain problem of a thin piezoceramic actuator sheet bonded to a homogeneous and isotropic elastic half plane through a thin bonding layer, as illustrated in Fig. 3.1. The host medium is modeled as a half plane to represent the case where it is much thicker than the actuator. The lengths of both the actuator and the bonding layer are denoted as $2a$, and the thicknesses of the actuator and the bonding layer are denoted as h and h', respectively. It is assumed that the poling direction of the actuator is along the z-axis. An electrical field E_z is applied along the poling direction of the actuator by applying a voltage (V) between the upper and the lower electrodes of the actuator with $E_z = V/h = (V^- - V^+)/h$. Throughout this chapter, superscripts a, b and h are used to designate physical quantities that belong to the actuator, the bonding layer and the host, respectively.

3.2.1 The actuator

Since the present study is focusing on a thin-sheet actuator with relatively small thickness in comparison with its length, σ_y^a and u_y^a are assumed to be uniform across its thickness, and σ_z^a and σ_{yz}^a in the actuator can be ignored [1]. Considering the fact that the bonding layer is much thinner than the actuator, it is assumed that the axial stress and deformation are uniform across the thickness of the bonding layer as well. The interfacial shear stress between different layers is denoted as τ, as shown in Fig. 3.1 with u^+ and u^- representing the displacements on the upper and lower surface of the bonding layer,

[1] The existence of τ will cause a non-zero σ_{yz}^a, but it represents a high order term of h, therefore it can be ignored if only thin actuator is considered.

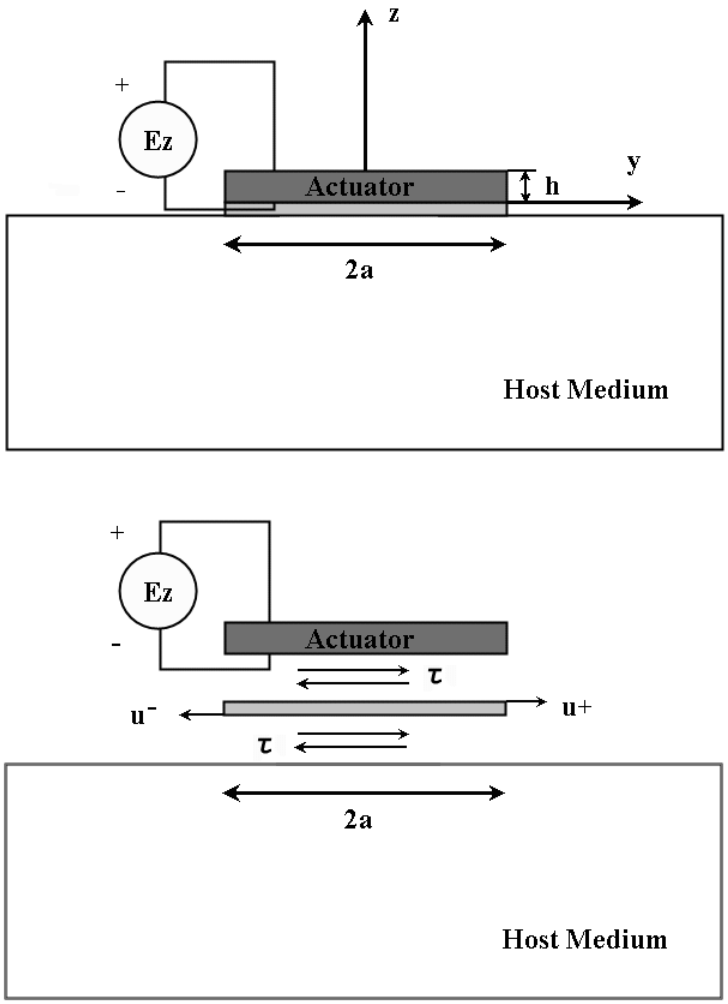

Figure 3.1: Schematics of the actuator configuration.

respectively.

Based upon these assumptions, the actuator can be modelled as an electroelastic line subjected to the applied electric field and distributed axial force, τ/h, as shown in Fig. 3.1. The equilibrium equation of the actuator can then be expressed as

$$\frac{d\sigma_y^a(y)}{dy} + \frac{\tau(y)}{h} = 0 \tag{3.1}$$

Since all the load transferred between the actuator and the bonding layer can be attributed to τ, the two ends of the actuator can be assumed to be traction free, i.e.

$$\sigma_y^a = 0, \quad |y| = a \tag{3.2}$$

By integrating Eq. (3.1) and making use of Eq. (3.2), the axial stress in the actuator can be expressed in terms of the shear stress τ as

$$\sigma_y^a(y) = -\int_{-a}^{y} \frac{\tau(\xi)}{h} d\xi \tag{3.3}$$

with

$$\int_{-a}^{a} \tau(\xi) d\xi = 0 \tag{3.4}$$

The axial stress of the actuator can be expressed in terms of the axial strain ϵ_y^a and the electric field E_z by using the following general constitutive relation:

$$\sigma_y^a(y) = E^a \epsilon_y^a(y) - e^a E_z \tag{3.5}$$

where E^a and e^a are effective material constants [20].

The resulting axial strain ϵ_y^a and displacement u_y^a can then be expressed in

terms of τ as

$$\epsilon_y^a(y) = -\frac{1}{E^a h}\int_{-a}^{y}\tau(\xi)d\xi + \frac{e^a E_z}{E^a}, \quad |y| < a \tag{3.6}$$

$$u_y^a(y) = -\frac{1}{E^a h}\int_{-a}^{y}(y-\xi)\tau(\xi)d\xi + \frac{e^a E_z y}{E^a}, \quad |y| < a \tag{3.7}$$

3.2.2 The bonding layer

The adhesive layer, formed by epoxy or conductive epoxy for example, is generally much more compliant than the host structure. Since the deformation of the actuator is transferred totally through the adhesive layer, the mechanical and geometrical properties of the adhesive layers will have a significant effect upon the performance of the integrated structure.

The shear stress τ distributed in the layer is determined by the constitutive relation:

$$-\tau(y) = \mu^b \varepsilon_y^b(y) \tag{3.8}$$

where

$$\varepsilon_y^b(y) = \frac{u^+(y) - u^-(y)}{h'} \tag{3.9}$$

with μ^b and ε_y^b being the shear modulus and the shear strain of the bonding layer, respectively. According to the continuity condition of the displacements, u^+ and u^- also represent the longitudinal displacements of the lower surface of the actuator and the upper surface of the host medium, respectively.

3.2.3 The host medium

Since there is no additional mechanical load applied to the host medium, the stress field generated inside the host structure is only due to the existence of

the shear stress caused by the actuator at the top of its surface. Therefore, the boundary condition along the top surface will be

$$\sigma_{yz}(y,0) = \begin{cases} -\tau(y) & |y| < a \\ 0 & |y| > a \end{cases}, \quad \sigma_z(y,0) = 0 \tag{3.10}$$

Making use of the fundamental solution of a half elastic plane subjected to a concentrated horizontal force [87] and the superposition principle, ϵ_y^h and u_y^h resulting from the applied force given by Eq. (3.10) can be obtained as

$$\epsilon_y^h(y,0) = \frac{1-\nu^h}{\pi\mu^h}\int_{-a}^{a}\frac{\tau(\xi)}{y-\xi}d\xi, \quad |y| < a \tag{3.11}$$

$$u_y^h(y,0) = \frac{1-\nu^h}{\pi\mu^h}\int_{-a}^{y}\int_{-a}^{a}\frac{\tau(\xi)}{y-\xi}d\xi dy, \quad |y| < a \tag{3.12}$$

where ν^h and μ^h are the Poisson's ratio and the shear modulus of the host, respectively.

3.2.4 Static load transfer in a perfectly bonded piezoelectric actuator

Taking the derivative of both sides of Eq. (3.8) with respect to y gives

$$-\frac{d\tau(y)}{dy} = \mu^b\Big[\frac{\epsilon^+(y)-\epsilon^-(y)}{h'}\Big] \tag{3.13}$$

Substituting Eqs. (3.6) and (3.11) into Eq. (3.13), the following integral equation can be obtained

$$\frac{1-\nu^h}{\pi\mu^h}\int_{-a}^{a}\frac{\tau(\xi)}{y-\xi}d\xi + \frac{1}{hE^a}\int_{-a}^{y}\tau(\xi)d\xi - \frac{h'}{\mu^b}\frac{d\tau(y)}{dy} = \frac{e^aE_z}{E^a}, \quad |y| < a \tag{3.14}$$

from which the shear stress τ can be determined.

Eqs. (3.14) and (3.4) can be normalized as

$$\left.\begin{aligned} \frac{1}{q}\int_{-1}^{1}\frac{\overline{\tau}(\zeta)d\zeta}{\eta-\zeta}+\frac{1}{v}\int_{-1}^{\eta}\overline{\tau}(\zeta)d\zeta-\frac{v'}{q'}\frac{d\overline{\tau}(\eta)}{d\eta}=1, \quad |\eta|<1 \\ \int_{-1}^{1}\overline{\tau}(\zeta)d\zeta=0 \end{aligned}\right\} \tag{3.15}$$

where

$$\overline{\tau}(\eta)=\frac{\tau(a\eta)}{e^a E_z}, \quad \eta=\frac{y}{a} \tag{3.16}$$

and

$$q=\frac{\pi E^h}{2[1-(\nu^h)^2]E^a}, \; v=\frac{h}{a}, \; q'=\frac{\mu^b}{E^a}, \; v'=\frac{h'}{a} \tag{3.17}$$

In the limiting case that the thickness of the bonding layer tends to zero, the third term in Eq. (3.15) disappears, and Eq. (3.15) reduces to

$$\left.\begin{aligned} \frac{1}{q}\int_{-1}^{1}\frac{\overline{\tau}(\zeta)d\zeta}{\eta-\zeta}+\frac{1}{v}\int_{-1}^{\eta}\overline{\tau}(\zeta)d\zeta=1, \quad |\eta|<1 \\ \int_{-1}^{1}\overline{\tau}(\zeta)d\zeta=0 \end{aligned}\right\} \tag{3.18}$$

which is a singular integral equation of the first kind [20]. The solution of it involves a square-root singularity at $|\eta|=1$ [87], which corresponds to the two ends of the actuator. For the case where a bonding layer exists, the solution of Eq. (3.15) has no singularity at $|\eta|=1$, indicating that introducing the bonding layer may lead to lower stress concentration and more uniform distribution of stress.

The general solutions of $\overline{\tau}$ in Eq. (3.15) can be expressed in terms of the

following expansions of Chebyshev polynomials

$$\overline{\tau}(\eta) = \frac{1}{\sqrt{1-\eta^2}} \sum_{j=0}^{\infty} d_j T_j(\eta) \tag{3.19}$$

where T_j are Chebyshev polynomials of the first kind with $T_j(\eta) = \cos(j\theta)$ and $\cos\theta = \eta$. By truncating the Chebyshev polynomial expansions to the Nth term and considering the boundary conditions at the following collocation points along the actuator

$$\eta_k = \cos\frac{k}{N+1}\pi, \quad k = 1, 2, \cdots, N \tag{3.20}$$

Eq. (3.15) reduces to

$$\sum_{j=1}^{N} d_j \frac{\sin\left(j\frac{k}{N+1}\pi\right)}{\sin\left(\frac{k}{N+1}\pi\right)} \left\{ \frac{1}{q} + \frac{1}{v\pi j}\sin\left(\frac{k}{N+1}\pi\right) + \frac{v'}{\pi q'}\left[\frac{j + \cot\left(j\frac{k}{N+1}\pi\right)\cot\left(\frac{k}{N+1}\pi\right)}{\sin\left(\frac{k}{N+1}\pi\right)} \right] \right\} = -\frac{1}{\pi}, \quad k = 1, 2, \cdots, N \tag{3.21}$$

The unknown coefficients d_j and the stress field due to the presence of the actuator can be readily determined by using Eq. (3.21).

3.2.5 Effect of interfacial debonding

The high level of shear stress at the edges of the actuator may result in an unwanted edge debonding as shown in Fig. 3.2. For a perfectly bonded actuator, when the maximum shear stress is larger than the bonding strength, edge debonding may develop. The debonded part of the actuator has zero boundary stresses. According to the present actuator model, the debonded part at the

edge of the actuator will experience no stress. As a result, the effective length of the actuator is reduced from its original length to that of the bonded part only. Therefore, the behaviour of an edge debonded actuator can be simulated by a shorter actuator [20].

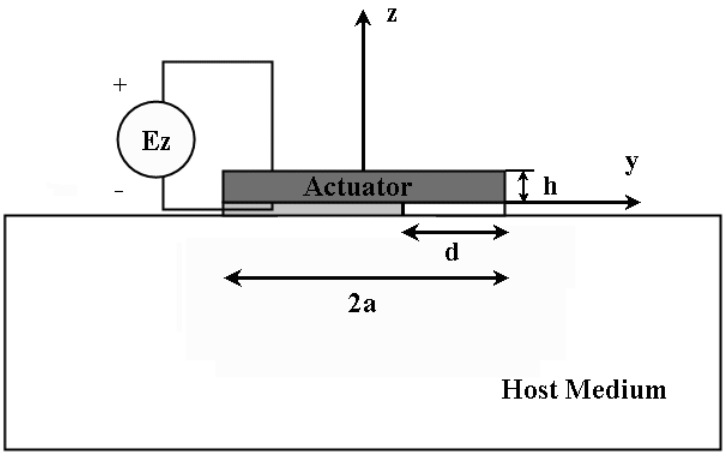

Figure 3.2: Schematics of edge debonding.

Debonding may also occur in the interior of the actuator. Let us consider an actuator occupying the region $t_l < y < t_r$ which is partially debonded in $d_l < y < d_r$ as illustrated in Fig. 3.3(a). The debonded part of the actuator can be regarded as a one-dimensional element subjected to an axial stress σ_d. By making use of the equilibrium equation Eq. (3.1) and the traction free condition at the two ends of the actuator, the axial stress in the actuator can be expressed in terms of τ as

$$\sigma_y^a(y) = \begin{cases} -\displaystyle\int_{t_l}^{y} \frac{\tau(\xi)}{h} d\xi & t_l < y < d_l \\ \sigma_d & d_l < y < d_r \\ \sigma_d - \displaystyle\int_{d_r}^{y} \frac{\tau(\xi)}{h} d\xi & d_r < y < t_r \end{cases} \tag{3.22}$$

where

$$\sigma_d = -\int_{t_l}^{d_l} \frac{\tau(\xi)}{h} d\xi \tag{3.23}$$

The partially debonded actuator can then be regarded as two "actuators" subjected to an axial stress σ_d at the inner tips of them, as shown in Fig. 3.3(b). The resulting axial strain can then be expressed in terms of τ as

$$\epsilon_y^a(y) = \begin{cases} -\dfrac{1}{E^a h} \displaystyle\int_{t_l}^{y} \tau(\xi) d\xi + \frac{e^a}{E^a} E_z & t_l < y < d_l \\ \dfrac{\sigma_d + e^a E_z}{E^a} & d_l < y < d_r \\ \dfrac{1}{E^a h} \Big[\sigma_d h - \displaystyle\int_{d_r}^{y} \tau(\xi) d\xi \Big] + \frac{e^a}{E^a} E_z & d_r < y < t_r \end{cases} \tag{3.24}$$

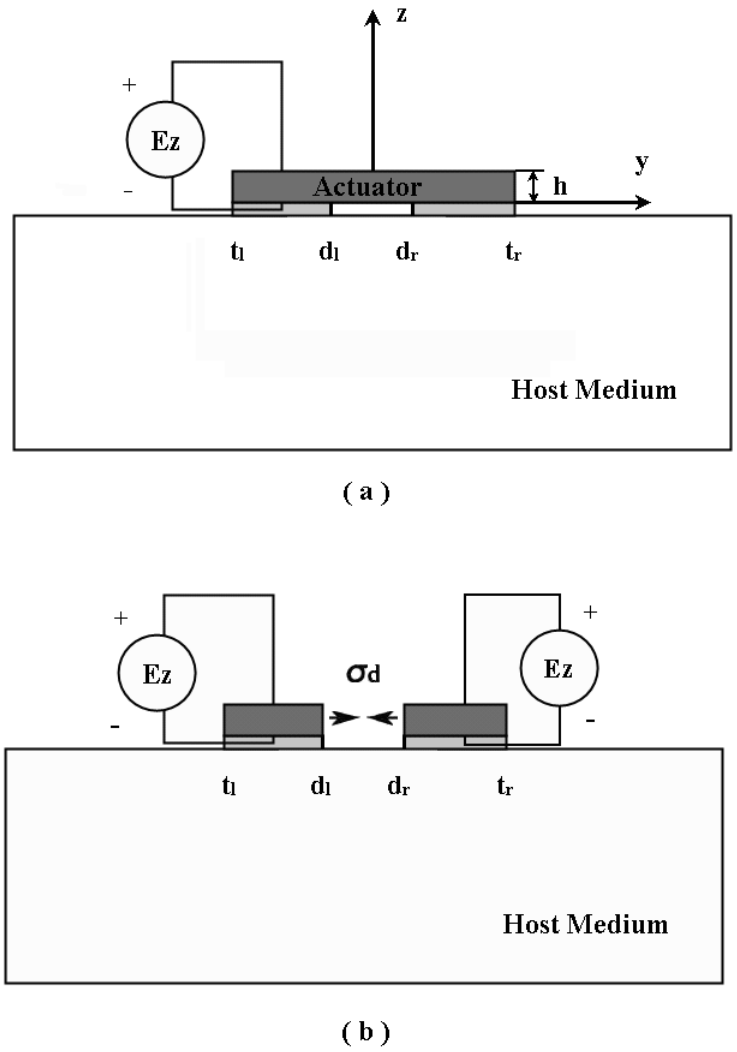

Figure 3.3: Schematics of interior debonding.

The half plane to which the actuator is bonded is subjected to the following boundary conditions:

$$\sigma_{yz}(y,0) = \begin{cases} -\tau(y) & t_l < y < d_l \ \text{ and } \ d_r < y < t_r \\ \\ 0 & \text{otherwise} \end{cases} \tag{3.25}$$

The surface strain in the host medium can be obtained, by making use of the fundamental solution of a half plane subjected to a concentrated surface force, as

$$\epsilon_y^h(y,0) = \frac{1-\nu^h}{\pi\mu^h}\Big[\int_{t_l}^{d_l} \frac{\tau(\xi)}{y-\xi}d\xi + \int_{d_r}^{t_r} \frac{\tau(\xi)}{y-\xi}d\xi\Big] \tag{3.26}$$

By making use of the constitutive relation of the bonding layer given by Eqs. (3.8) and (3.9), the strains in the actuator and the host medium presented by Eqs. (3.24) and (3.26) can be related as

$$\epsilon_y^a - \epsilon_y^h = -\frac{h'}{\mu^b}\frac{d\tau(y)}{dy} \quad t_l < y < d_l, \quad d_r < y < t_r, \quad z = 0 \tag{3.27}$$

Substituting Eqs. (3.24) and (3.26) into Eq. (3.27) gives

$$\begin{aligned} &\frac{1-\nu^h}{\pi\mu^h}\int_{t_l}^{d_l} \frac{\tau(\xi)}{y-\xi}d\xi + \frac{1-\nu^h}{\pi\mu^h}\int_{d_r}^{t_r} \frac{\tau(\xi)}{y-\xi}d\xi - \frac{h'}{\mu^b}\frac{d\tau(y)}{dy} \\ &+ \begin{cases} \dfrac{1}{hE^a}\displaystyle\int_{t_l}^{y}\tau(\xi)d\xi = \frac{e^aE_z}{E^a} & t_l < y < d_l \\ \\ \dfrac{1}{hE^a}\displaystyle\int_{d_r}^{y}\tau(\xi)d\xi = \frac{e^aE_z+\sigma_d}{E^a} & d_r < y < t_r \end{cases} \end{aligned} \tag{3.28}$$

The axial stress σ_d in Eq. (3.28) need to be determined by considering the

deformation of the debonded part of the actuator. From Eqs. (3.8) and (3.9) it can be obtained that

$$u_y^a(d_r) - u_y^a(d_l) = u_y^h(d_r) - u_y^h(d_l) + \frac{h'}{\mu^b}[\tau(d_l) - \tau(d_r)] \tag{3.29}$$

Integrating Eqs. (3.24) and (3.26) gives

$$u_y^a(d_r) - u_y^a(d_l) = \frac{\sigma_d + e^a E_z}{E^a}(d_r - d_l) \tag{3.30}$$

$$u_y^h(d_r) - u_y^h(d_l) = \frac{1-\nu^h}{\pi\mu^h}\int_{d_l}^{d_r}\Big[\int_{t_l}^{d_l}\frac{\tau(\xi)}{y-\xi}d\xi + \int_{d_r}^{t_r}\frac{\tau(\xi)}{y-\xi}d\xi\Big]dy \tag{3.31}$$

Substituting Eqs. (3.30) and (3.31) into Eq. (3.29), the following equation can be obtained, which provides an additional condition for determining σ_d.

$$\begin{aligned}\frac{1-\nu^h}{\pi\mu^h}\int_{d_l}^{d_r}\Big[\int_{t_l}^{d_l}\frac{\tau(\xi)}{y-\xi}d\xi + \int_{d_r}^{t_r}\frac{\tau(\xi)}{y-\xi}d\xi\Big]dy + \frac{h'}{\mu^b}[\tau(d_l) - \tau(d_r)] \\ = \frac{\sigma_d + e^a E_z}{E^a}(d_r - d_l)\end{aligned} \tag{3.32}$$

Eqs. (3.23), (3.28) and (3.32) can be normalized as

$$\begin{aligned}&\frac{1}{q}\int_{-1}^{1}\frac{\tau^l(\zeta)d\zeta}{\eta_l-\zeta} + \frac{1}{q}\int_{-1}^{1}\frac{\tau^r(\zeta)d\zeta}{\eta_r-\zeta} \\ &+\begin{cases} -\dfrac{v_l'}{q'}\dfrac{d\tau^l(\eta_l)}{d\eta_l} + \dfrac{1}{v_l}\displaystyle\int_{-1}^{\eta_l}\tau^l(\zeta)d\zeta = 1 & |\eta_l| < 1 \\ -\dfrac{v_r'}{q'}\dfrac{d\tau^r(\eta_r)}{d\eta_r} - \dfrac{1}{v_r}\displaystyle\int_{\eta_r}^{1}\tau^r(\zeta)d\zeta = 1 & |\eta_r| < 1 \end{cases}\end{aligned} \tag{3.33}$$

$$\begin{aligned}&\frac{1}{v_l}\int_1^{\eta_l^*}\int_{-1}^{1}\frac{\tau^l(\zeta)d\zeta}{\eta_l-\zeta}d\eta_l + \frac{1}{v_r}\int_{\eta_r^*}^{-1}\int_{-1}^{1}\frac{\tau^r(\zeta)d\zeta}{\eta_r-\zeta}d\eta_r + \frac{qv_l'}{q'v_l}\tau^l(1) - \frac{qv_r'}{q'v_r}\tau^r(-1) \\ &\qquad = 2q\Big(\frac{1}{v} - \frac{1}{v_l} - \frac{1}{v_r}\Big)(\sigma^* + 1)\end{aligned} \tag{3.34}$$

and

$$\int_{-1}^{1} \tau^l(\zeta) d\zeta = -\sigma^* v_l \tag{3.35}$$

$$\int_{-1}^{1} \tau^r(\zeta) d\zeta = \sigma^* v_r \tag{3.36}$$

where the normalized stresses are given by

$$\tau^l(\eta_l) = \frac{\tau(a_l \eta_l + y_l)}{e^a E_z}, \quad \tau^r(\eta_r) = \frac{\tau(a_r \eta_r + y_r)}{e^a E_z}, \quad \sigma^* = \frac{\sigma_d}{e^a E_z} \tag{3.37}$$

with

$$\left.\begin{gathered} \eta_l = \frac{y - y_l}{a_l}, \quad \eta_r = \frac{y - y_r}{a_r} \\ v = \frac{h}{a}, \; v_l = \frac{h}{a_l}, \; v_r = \frac{h}{a_r} \\ v' = \frac{h'}{a}, \; v_l' = \frac{h'}{a_l}, \; v_r' = \frac{h'}{a_r} \\ a = \frac{1}{2}(t_r - t_l), \; a_l = \frac{1}{2}(d_l - t_l), \; a_r = \frac{1}{2}(t_r - d_r) \\ y_l = \frac{1}{2}(d_l + t_l), \; y_r = \frac{1}{2}(t_r + d_r) \\ \eta_l^* = 2v_l \frac{v_r - v}{v_r v} - 1, \quad \eta_r^* = -2v_r \frac{v_l - v}{v_l v} + 1 \end{gathered}\right\} \tag{3.38}$$

The general solutions of τ^l and τ^r in Eqs. (3.33)–(3.36) can then be expressed in terms of the following expansions of Chebyshev polynomials

$$\tau^l(\eta_l) = \frac{1}{\sqrt{1 - \eta_l^2}} \sum_{j=0}^{\infty} d_j^l T_j(\eta_l), \quad \tau^r(\eta_r) = \frac{1}{\sqrt{1 - \eta_r^2}} \sum_{j=0}^{\infty} d_j^r T_j(\eta_r) \tag{3.39}$$

If the Chebyshev polynomial expansions are truncated to the Nth term, and Eq. (3.33) is satisfied at the following collocation points at each bonded

segment of the actuator given by

$$\eta_{lk} = \eta_{rk} = \eta_k = \cos\frac{k}{N+1}\pi, \quad k = 1, 2, \cdots, N \tag{3.40}$$

Eqs. (3.33) and (3.34) reduce to

$$\begin{aligned}
&\sum_{j=1}^{N} d_j^l \frac{\sin\left(j\frac{k}{N+1}\pi\right)}{\sin\left(\frac{k}{N+1}\pi\right)}\left\{\frac{1}{q} + \frac{1}{v_l \pi j}\sin\left(\frac{k}{N+1}\pi\right)\right. \\
&\qquad \left. + \frac{v_l'}{\pi q'}\left[\frac{j + \cot\left(j\frac{k}{N+1}\pi\right)\cot\left(\frac{k}{N+1}\pi\right)}{\sin\left(\frac{k}{N+1}\pi\right)}\right]\right\} \\
&+\sum_{j=1}^{N} d_j^r \frac{\left[\sqrt{(\eta_{rk}')^2 - 1} - |\eta_{rk}'|\right]^j}{q\sqrt{(\eta_{rk}')^2 - 1}} + \frac{\sigma^*}{\pi}\left[\frac{v_r}{q\sqrt{(\eta_{rk}')^2 - 1}} + \left(1 - \frac{k}{N+1}\right)\right. \\
&\qquad \left. - \frac{v_l' v_l}{\pi q'}\frac{\cot\left(\frac{k}{N+1}\pi\right)}{\sin^2\left(\frac{k}{N+1}\pi\right)}\right] = -\frac{1}{\pi}, \quad k = 1, 2, \cdots, N
\end{aligned} \tag{3.41}$$

$$\begin{aligned}
&\sum_{j=1}^{N} d_j^r \frac{\sin\left(j\frac{k}{N+1}\pi\right)}{\sin\left(\frac{k}{N+1}\pi\right)}\left\{\frac{1}{q} + \frac{1}{v_r \pi j}\sin\left(\frac{k}{N+1}\pi\right)\right. \\
&\qquad \left. + \frac{v_r'}{\pi q'}\left[\frac{j + \cot\left(j\frac{k}{N+1}\pi\right)\cot\left(\frac{k}{N+1}\pi\right)}{\sin\left(\frac{k}{N+1}\pi\right)}\right]\right\} \\
&-\sum_{j=1}^{N} d_j^l (-1)^j \frac{\left[\sqrt{(\eta_{lk}')^2 - 1} - |\eta_{lk}'|\right]^j}{q\sqrt{(\eta_{lk}')^2 - 1}} + \frac{\sigma^*}{\pi}\left[\frac{v_l}{q\sqrt{(\eta_{lk}')^2 - 1}} + \frac{k}{N+1}\right. \\
&\qquad \left. + \frac{v_r' v_r}{\pi q'}\frac{\cot\left(\frac{k}{N+1}\pi\right)}{\sin^2\left(\frac{k}{N+1}\pi\right)}\right] = -\frac{1}{\pi}, \quad k = 1, 2, \cdots, N
\end{aligned} \tag{3.42}$$

$$
\begin{aligned}
&-\sigma^*\Bigg[\frac{1}{q}\ln|\eta_l^*+\sqrt{\eta_l^{*2}-1}|-\frac{1}{q}\ln|\eta_r^*+\sqrt{\eta_r^{*2}-1}| \\
&\qquad +2\Big(\frac{1}{v}-\frac{1}{v_l}-\frac{1}{v_r}\Big)+\frac{v_r'+v_l'}{\pi q'\sin\Big(\dfrac{1}{N+1}\pi\Big)}\Bigg] \\
&+\sum_{j=1}^{N}\frac{d_j^l}{v_l}\Bigg\{\pi(-1)^j\int_1^{\eta_l^*}\frac{\Big[\sqrt{(\eta_{lk}')^2-1}-|\eta_{lk}'|\Big]^j}{q\sqrt{(\eta_{lk}')^2-1}}d\eta_{lk}'+\frac{v_l'}{q'}\frac{\cos\Big(j\dfrac{1}{N+1}\pi\Big)}{\sin\Big(\dfrac{1}{N+1}\pi\Big)}\Bigg\} \\
&+\sum_{j=1}^{N}\frac{d_j^r}{v_r}\Bigg\{-\pi\int_{\eta_r^*}^{-1}\frac{\Big[\sqrt{(\eta_{rk}')^2-1}-|\eta_{rk}'|\Big]^j}{q\sqrt{(\eta_{rk}')^2-1}}d\eta_{rk}'-(-1)^j\frac{v_r'}{q'}\frac{\cos\Big(j\dfrac{1}{N+1}\pi\Big)}{\sin\Big(\dfrac{1}{N+1}\pi\Big)}\Bigg\} \\
&\qquad =2\Big(\frac{1}{v}-\frac{1}{v_l}-\frac{1}{v_r}\Big) \qquad (3.43)
\end{aligned}
$$

where

$$\eta'_{lk}=v_l\Big(\frac{2}{v}-\frac{1}{v_l}-\frac{1}{v_r}+\frac{1}{v_r}\cos\frac{k}{N+1}\pi\Big) \qquad (3.44)$$

$$\eta'_{rk}=-v_r\Big(\frac{2}{v}-\frac{1}{v_l}-\frac{1}{v_r}-\frac{1}{v_l}\cos\frac{k}{N+1}\pi\Big) \qquad (3.45)$$

The unknown coefficients d_j^l, d_j^r and σ^* can be determined by solving Eqs. (3.41)–(3.43).

3.3 Numerical Results and Discussion

In this section, the results of numerical simulation of the influence of the property of the bonding layer under different material combinations and actuator geometries on the electromechanical behaviour of the integrated system are presented. The attention is focused on the shear stress distribution along the bonding layer. The convergence of the solution using Chebyshev polynomials

has been carefully evaluated. The number of terms of Chebyshev polynomials is selected to be 64, with which the convergence of the results for all the cases considered is ensured.

The normalized interfacial shear stress $\tau^* = \tau/e^a E_z$ is an important indicator of the actuation efficiency, and represents the load transfer between the actuator and the host medium. Fig. 3.4 shows a typical shear stress distribution of a surface bonded actuator for $q = 2.28$, $v = 0.2$ and $v' = 0$. To verify the validity of the present actuator model to predict the interfacial stress distribution, the ANSYS software was used to numerically analyze the stress field of the same problem using the real geometric configuration of the actuator. The comparison shows a limited discrepancy between the finite element and analytical results near the tips of the actuator. This discrepancy is caused by the use of different actuator models in the analyses. In the analytical work, one-dimensional representation was used to model the behaviour of the actuator, while in the finite element analysis a two-dimensional model was used. The current one-dimensional actuator model can be used to predict interfacial shear stress away from the tips of the actuator (two times of the thickness of the actuator, for example). It should be mentioned that most sheet-actuators have high length-to-thickness ratio. In these situations, the current explicit model can be used to predict the load transfer between the actuator and the host structure analytically in an efficient manner.

3.3.1 Actuator with a uniform interfacial layer

As shown in Eq. (3.17), q represents the material combination of the actuator and the host structure, v represents actuator geometry, q' represents material property of the bonding layer and v' represents the geometry of the bonding

Table 3.1: Material Properties of the Piezoelectric Actuator

Elastic Stiffness Parameters	c_{11}	c_{12}	c_{13}	c_{33}	c_{44}
(Pa)	13.9×10^{10}	6.78×10^{10}	7.43×10^{10}	11.5×10^{10}	2.56×10^{10}
Piezoelectric Constants	e_{31}	e_{33}	e_{15}		
(C/m^2)	-5.2	15.1	12.7		
Dielectric Constants	ϵ_{11}	ϵ_{33}			
(C/Vm)	6.45×10^{-9}	5.62×10^{-9}			

Table 3.2: Material Properties of the Host Medium and the Bonding Layer

Host Medium	
Young's Modulus E^h (Pa)	5.27×10^{10}
Poisson's Ratio ν^h	0.3
Bonding Layer	
Shear Modulus μ^b (Pa)	1.0×10^9

layer. Carefully examining Eq. (3.15) indicates that the normalized interfacial shear stress is governed by three parameters: q, v and v'/q'. In the following discussion, the values of q, v and v' are varied to evaluate different responses of the structure.

The piezoelectric material considered in the following examples is a typical piezoceramics, whose properties are given in Table 3.1 [88]. The properties of the bonding layer [7] and the host medium [89] are given in Table 3.2. From these material constants it can be determined that $q = 1.0$ and $q' = 0.011$. The geometry of the actuator is assumed to be $a = 1.0$ cm and $h = 200$–2000 μm. The length of the bonding layer is the same as that of the actuator.

Since the distribution of τ^* is anti-symmetrical about the middle point of $y = 0$, the stress distribution along only half of the actuator will be presented. The results for shear stress distribution along the bonding interface for $q = 1.0$

and $q' = 0.011$ with two bonding conditions, $v' = 0$ and $v' = 0.01$, are shown in Figs. 3.5 and 3.6, respectively. As shown in Fig. 3.5, the increase in the v value makes shear stress distribution less concentrated around the tips of the actuator. Increase of shear stress level along the actuator due to increasing v value is also observed. When a bonding layer is included, as shown in Fig. 3.6, the stress concentration around the tip of the actuator is dramatically reduced, yet on the other hand the shear stress level along the actuator is increased, in comparison with the corresponding curve in Fig. 3.5.

To study the effect of material mismatch q, the material constants of the actuator are fixed, and the shear modulus of the host medium is changed to achieve different material combinations. $q = 0.1$, 0.5, 1.0, 2.0 and 5.0 are chosen, and two bonding conditions, $v' = 0$ and $v' = 0.01$, are considered to investigate the effect of the material combination on the load transfer between the actuator and the host structure. The normalized shear stress distribution curves under these two bonding conditions are shown in Figs. 3.7 and 3.8, respectively. In Fig. 3.7, with the increase of q, an increase of the shear stress level at the tips of the actuator can be observed. Fig. 3.8 shows that when the bonding layer is included, the increase of q results in an increase of the shear stress level along the entire length of the actuator, and the shear stress distribution becomes less concentrated around the tips of the actuator. Figs. 3.5–3.8 indicate that the material mismatch and geometrical property of the actuator and the host structure show more significant effect on the shear stress distribution when the bonding layer is included, at least for the currently considered bonding layer. Proper selection of material combination and actuator geometry, if possible, will increase the actuation efficiency of the actuator.

Fig. 3.9 shows a typical shear stress distribution along a surface bonded actuator for $q = 1.0$, $v = 0.05$ and $q' = 0.011$. High stress concentration around the tip of the actuator is observed when $v' = 0$. Comparing the five curves in this figure, we can clearly see that, as the v' value increases from 0 to 0.02, the shear stress level along the actuator between the interval of $y/a = 0.0 \sim 0.9$ shows very limited changes, but the stress concentration around the tip of the actuator, where $y/a = 1.0$, decreases significantly.

3.3.2 Interfacial debonding

3.3.2.1 Edge debonding

For a perfectly bonded actuator, when the maximum shear stress is larger than the bonding strength, edge debonding will initiate and grow to a length d, as shown in Fig. 3.2. As mentioned in the last section, a debonded actuator can be regarded as a shorter actuator. The effective length of the actuator is reduced from its original length $2a$ to $2a_{eff} = 2a - d$.

To evaluate the effect of the thickness of the bonding layer in edge debonding problem, Fig. 3.10 shows the normalized shear stress τ^* at the edge point $\eta_e = y/a = -1$ as a function of d/a for $q = 1.0$, $q' = 0.011$ and $v = 0.05$. As expected when the debonding continues developing, the edge stresses decrease. When the edge stresses decrease to the values below the interfacial toughness, the debonding will stop growing. This is the self-arresting mechanism, which has been discussed by Refs. [20] and [28]. Fig. 3.10 shows that the increase of the debonding length, from $d = 0$ to $d = a$ for example, will decrease the shear stress $\tau^*(\eta_e)$ by up to 3% for $v' = 0.007$ and 12% for $v' = 0.025$, indicating that with the increase of the thickness of the bonding layer, the self-arresting effect becomes more obvious.

3.3.2.2 Central debonding

Local stress concentration and/or weak interfacial bonding may also result in debonding in the interior of the actuator as shown in Fig. 3.3. To simulate this situation, the actuator considered is assumed symmetrically debonded in $|y| < d$, i.e. $t_r = -t_l = a$ and $d_r = -d_l = d$. The effective length of the actuator is reduced from its original length $2a$ to $2a_{eff} = 2(a - d)$.

Shear stress redistributions along actuators with central debondings for $q = 1.0$, $q' = 0.011$ and $v = 0.05$ with two bonding conditions, $v' = 0$ and $v' = 0.01$, are shown in Figs. 3.11 and 3.12, respectively. Fig. 3.11 shows that when the bonding layer is ignored shear stresses concentrate near the debonding edge, particularly for larger debonding lengths; it may be detrimental to the bonding strength. Fig. 3.11 also shows that central debondings mainly cause the stress redistribution near the debonding area, and does not significantly affect stresses far away from the debonding. However, when the bonding layer is included as illustrated in Fig. 3.12, shear stresses do not concentrate in the debonding edge and show a much more uniform distribution.

The results for shear stress redistribution along a surface bonded actuator for $q = 1.0$, $q' = 0.011$ and $d/a = 0.6$ under two bonding conditions, $v' = 0$ and $v' = 0.01$, are shown in Figs. 3.13 and 3.14, respectively. High stress concentration at the debonding edge and increase of shear stress level along the actuator due to increasing v value are observed in Fig. 3.13. When a bonding layer is included, as shown in Fig. 3.14, the stress concentration around the tip of the actuator is dramatically reduced, and the parameter v has more effect on the shear stress distribution.

Fig. 3.15 shows a typical shear stress redistribution along a surface bonded actuator for $q = 1.0$, $q' = 0.011$, $v = 0.05$ and $d/a = 0.6$. The normalized

shear stresses at the edge points $\eta_{el} = y/a = d/a$ and $\eta_{er} = y/a = 1$ as a function of d/a are shown in Figs. 3.16 and 3.17, respectively. It is observed that the shear stress at the debonding edge is singular when $v' = 0$, yet as the v' value increases from 0 to 0.02, the concentration of the shear stress at the debonding edge is significantly reduced. When the debonding occurs in $d/a < 0.7$, the shear stresses at the debonding edges, $\tau^*(\eta_{er})$ and $\tau^*(\eta_{el})$, show a very limited change. When the interior debondings are developed in range of $0.7 < d/a < 1$, stress redistribution causes the shear stresses at the edge points to increase significantly. $\tau^*(\eta_{er})$, for example, increases by up to 27% for $v' = 0.002$ and 55% for $v' = 0.02$ at $d/a = 0.9$. The corresponding results of the axial stress in the debonded part of the actuator, σ^*, as a function of d/a is shown in Fig. 3.18. The thickness of the bonding layer does show significant effect upon the axial stress σ^* in the actuator. It should be mentioned, however, when the thickness of the layer is small compared with the thickness of the actuator, d/a shows insignificant effect until the debonding approaches the tip of the actuator. It is also interesting to observe that with the effect of the bonding layer, the axial stress in the debonded part of the actuator is more sensitive to the change of the debonding length, d/a, while the shear stress at the edge of the actuator is less sensitive to d/a in comparison with the case where no bonding layer exists.

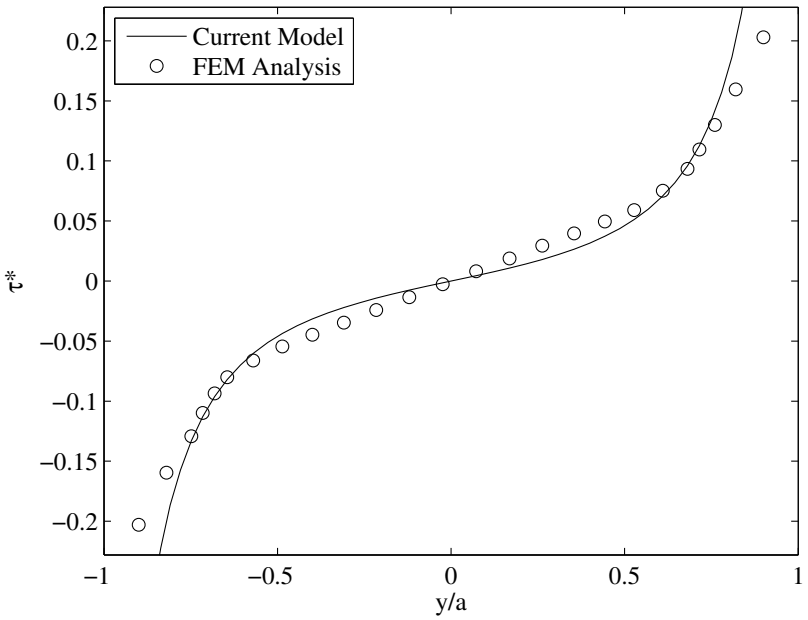

Figure 3.4: Interfacial shear stress distribution ($q = 2.28$, $v = 0.2$ and $v' = 0$). Solutions obtained from current model are shown as lines and FEA as data points.

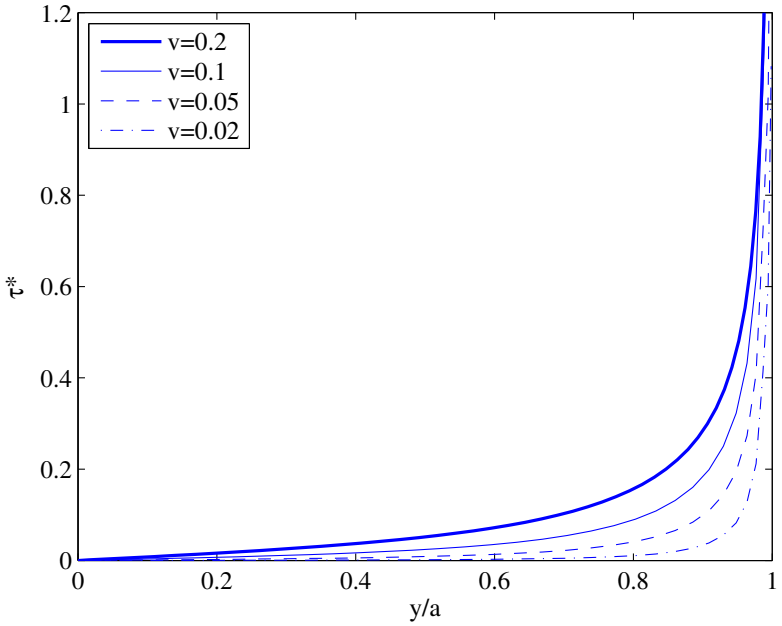

Figure 3.5: Interfacial shear stress distribution ($q = 1.0$ and $v' = 0$).

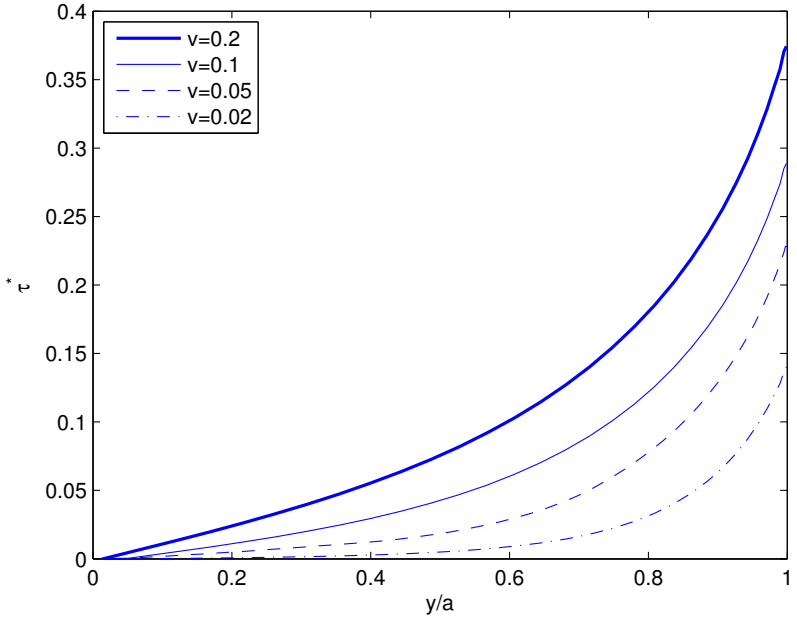

Figure 3.6: Interfacial shear stress distribution ($q = 1.0$, $q' = 0.011$ and $v' = 0.01$).

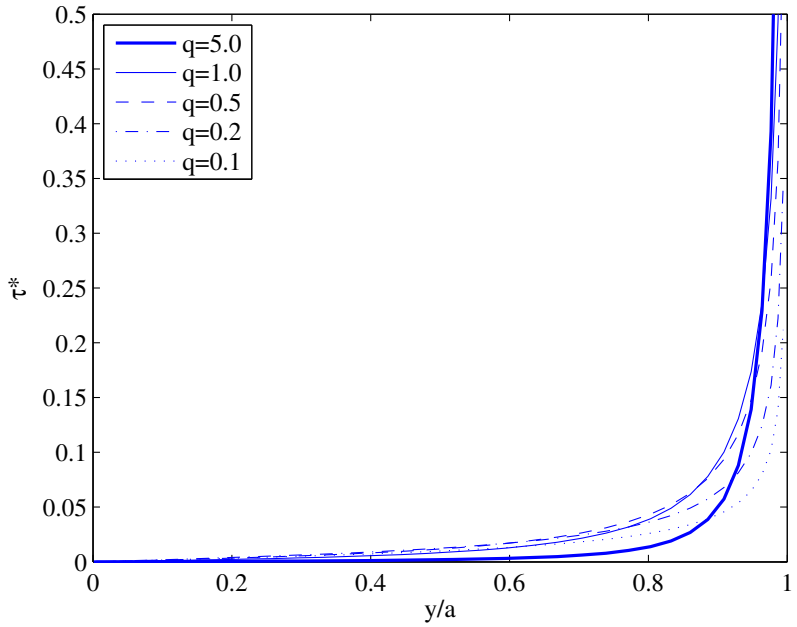

Figure 3.7: Interfacial shear stress distribution ($v = 0.05$ and $v' = 0$).

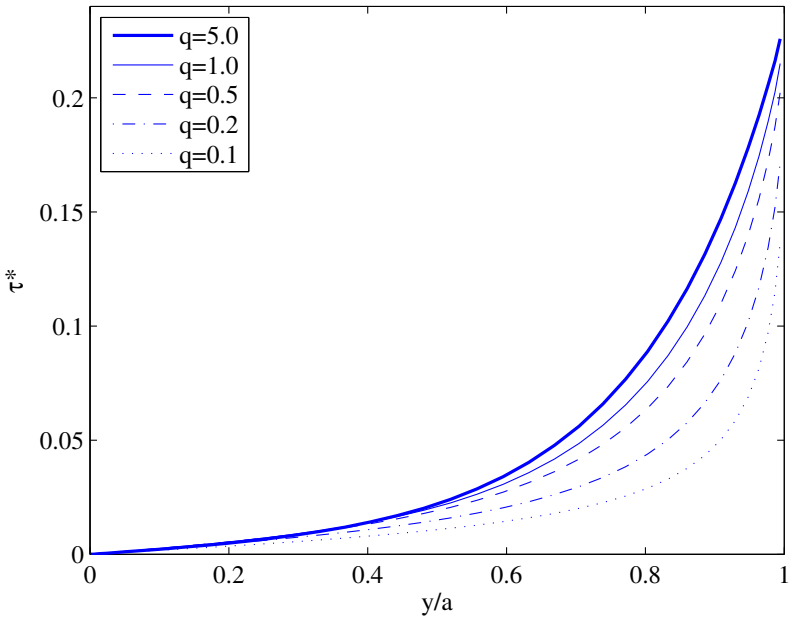

Figure 3.8: Interfacial shear stress distribution ($q' = 0.011$, $v = 0.05$ and $v' = 0.01$).

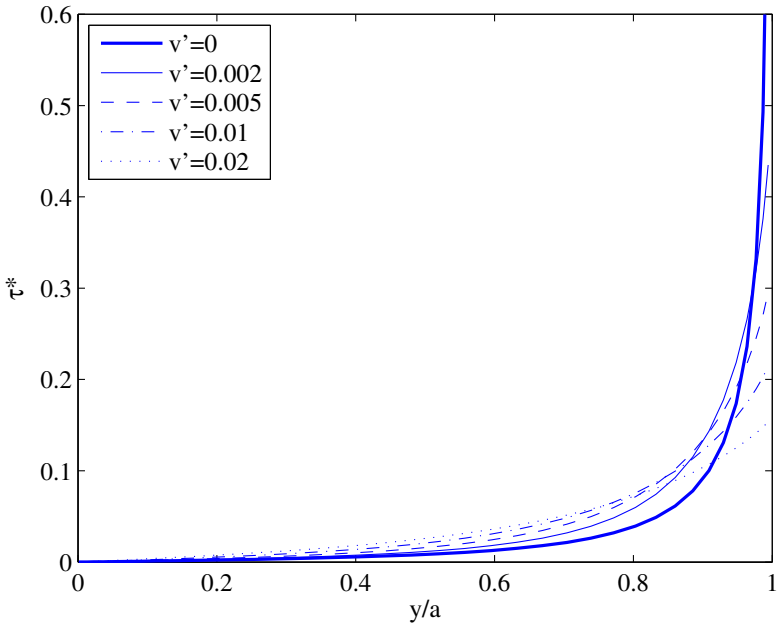

Figure 3.9: Interfacial shear stress distribution ($q = 1.0$, $q' = 0.011$ and $v = 0.05$).

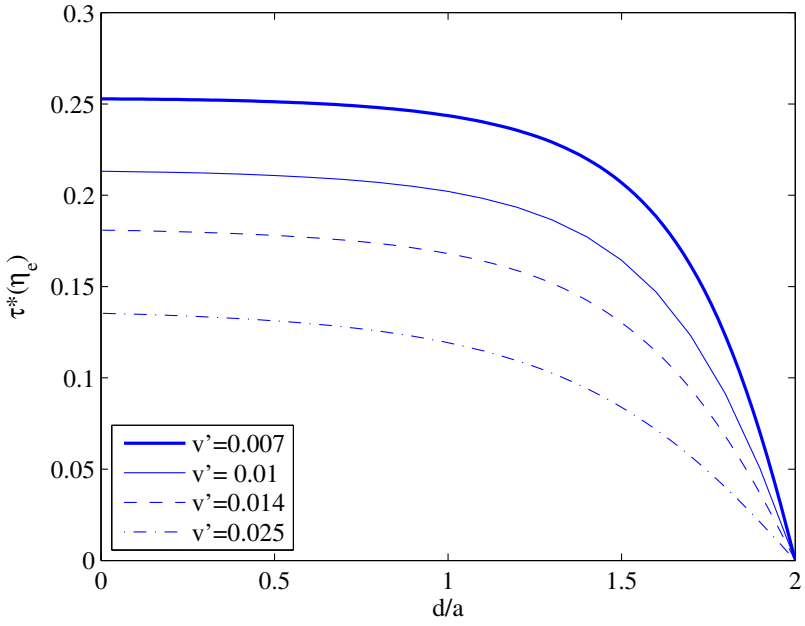

Figure 3.10: $\tau^*(\eta_e)$ as a function of d/a ($q = 1.0$, $q' = 0.011$ and $v = 0.05$).

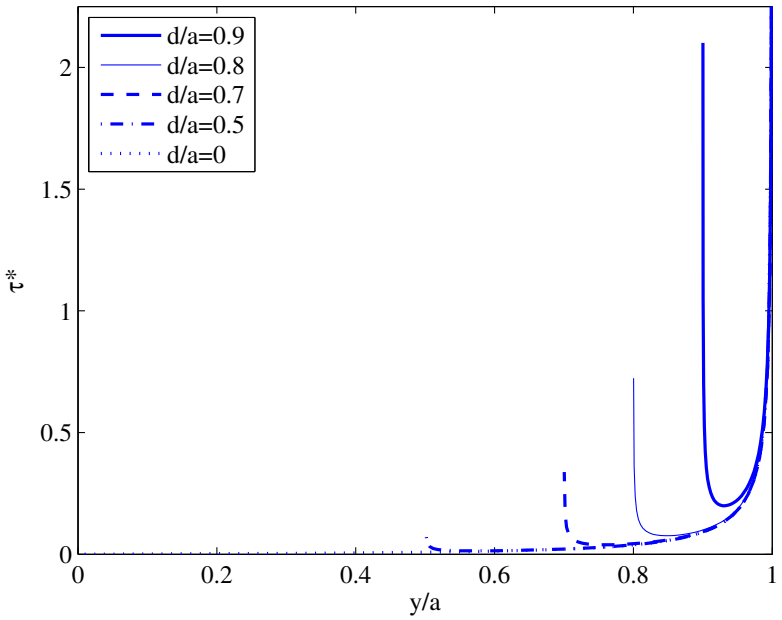

Figure 3.11: Interfacial shear stress distribution ($q = 1.0$, $v = 0.05$ and $v' = 0$).

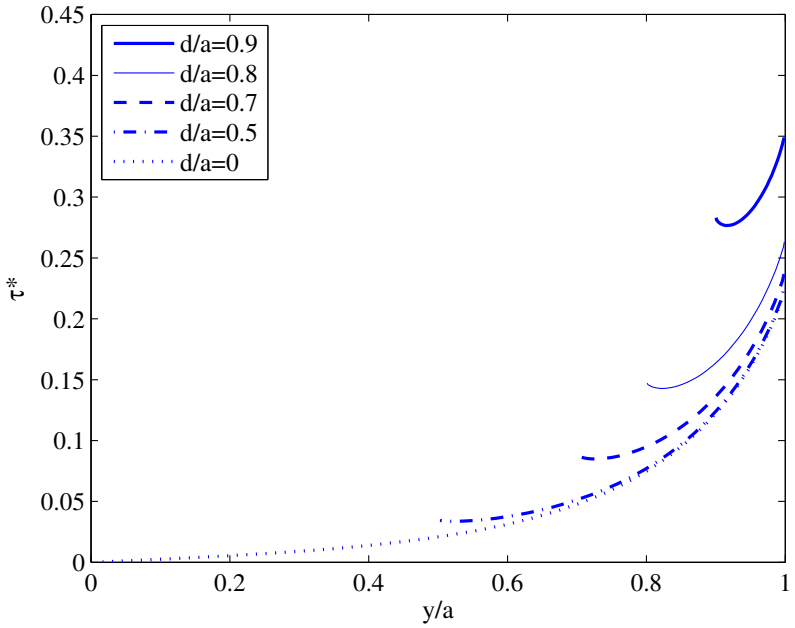

Figure 3.12: Interfacial shear stress distribution ($q = 1.0$, $q' = 0.011$, $v = 0.05$ and $v' = 0.01$).

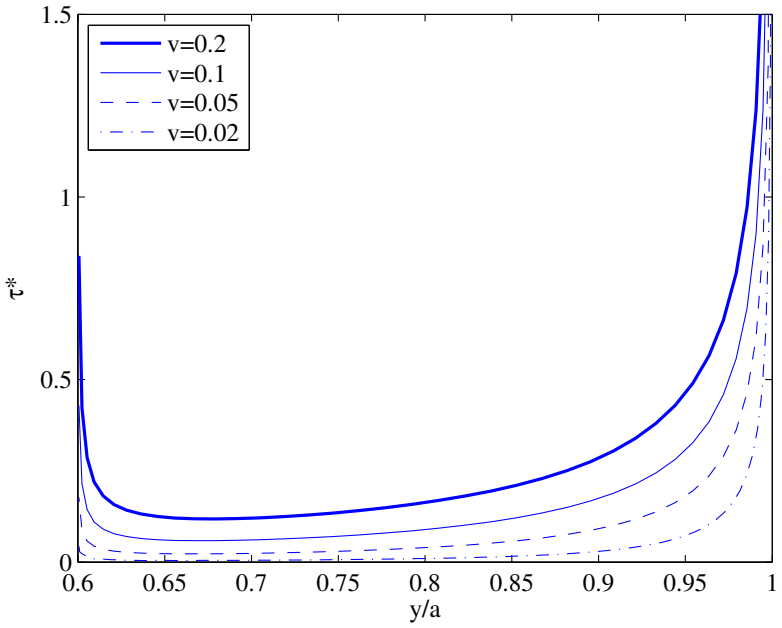

Figure 3.13: Interfacial shear stress distribution ($q = 1.0$, $d/a = 0.6$ and $v' = 0$).

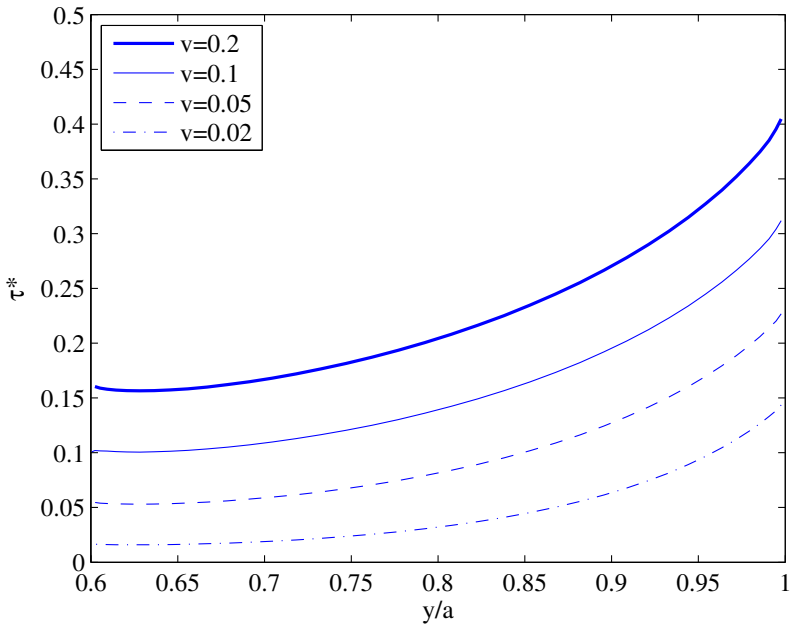

Figure 3.14: Interfacial shear stress distribution ($q = 1.0$, $q' = 0.011$, $d/a = 0.6$ and $v' = 0.01$).

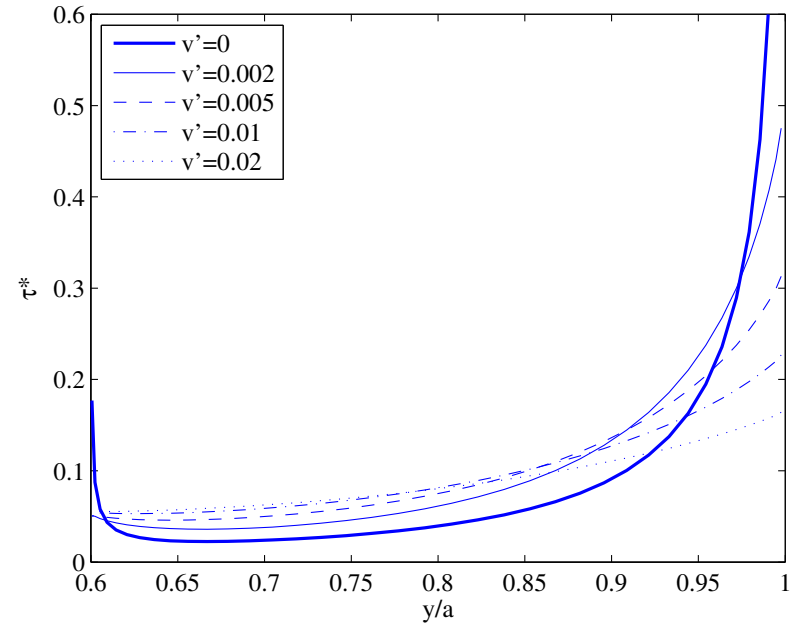

Figure 3.15: Interfacial shear stress distribution ($q = 1.0$, $q' = 0.011$, $v = 0.05$ and $d/a = 0.6$).

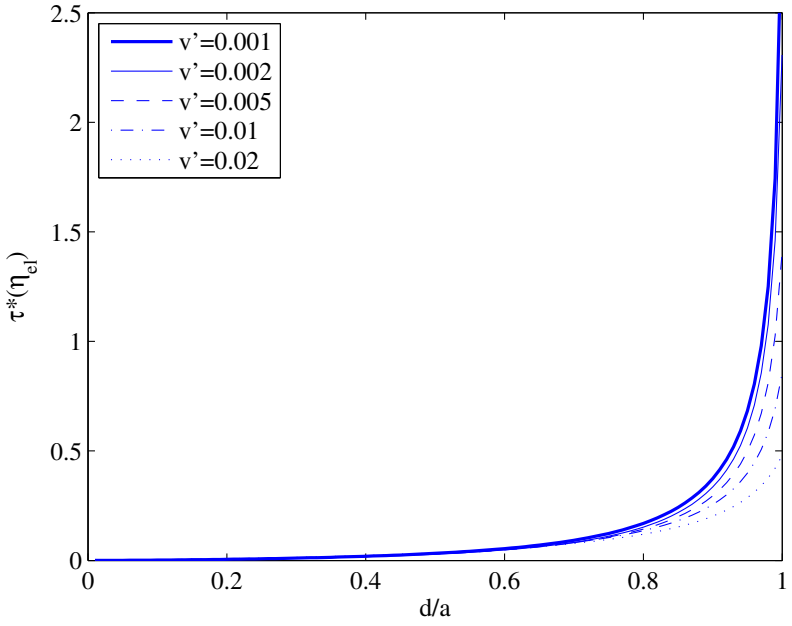

Figure 3.16: $\tau^*(\eta_{el})$ as a function of d/a ($q = 1.0$, $q' = 0.011$ and $v = 0.05$).

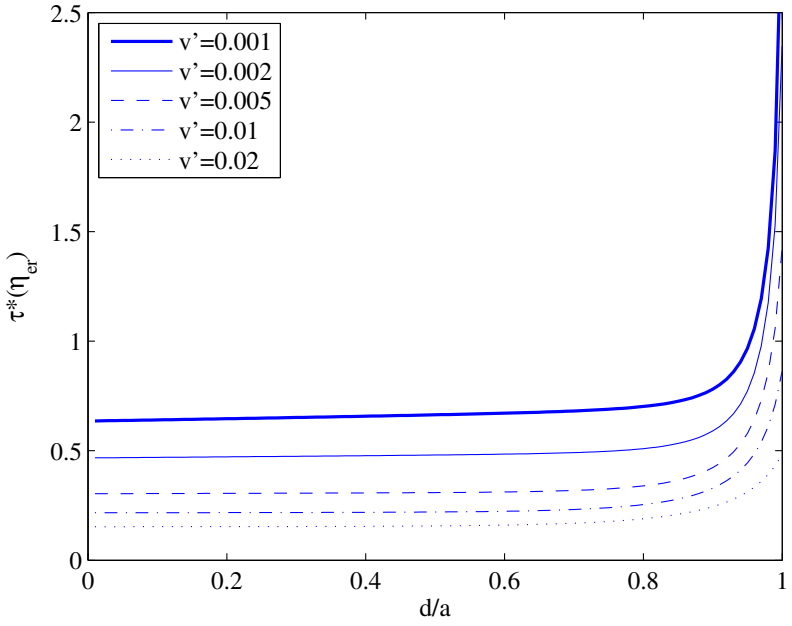

Figure 3.17: $\tau^*(\eta_{er})$ as a function of d/a ($q = 1.0$, $q' = 0.011$ and $v = 0.05$).

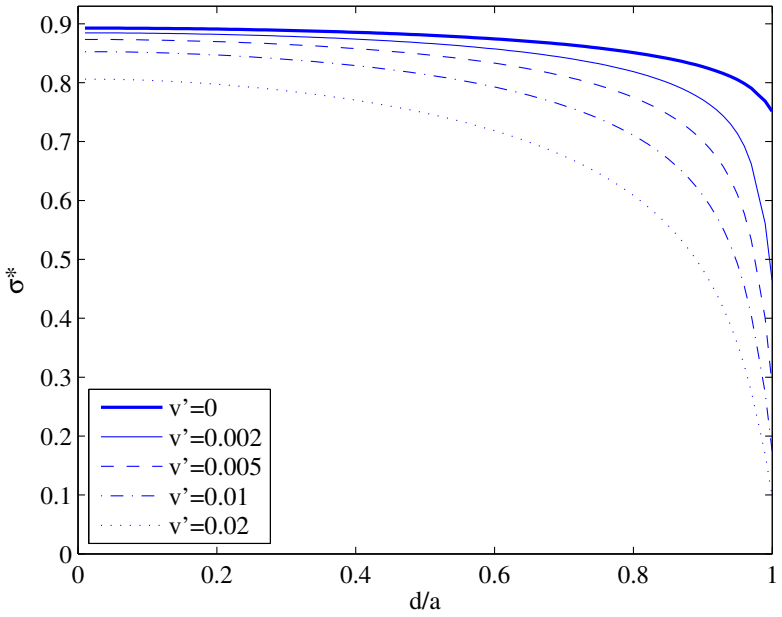

Figure 3.18: σ^* as a function of d/a ($q = 1.0$, $q' = 0.011$ and $v = 0.05$).

3.4 Concluding Remarks

The focus of this chapter is on the study of the effect of the material and geometric properties of the actuator and the bonding layer on the load transfer from the actuator to the host medium. A general analytical solution is provided to the coupled electromechanical behaviour of a piezoelectric actuator bonded to a host through an adhesive bonding layer under plane electric loading. The validity of the present model has been demonstrated by application to specific examples and comparison with the correspond results obtained from Finite Element method. The numerical investigation of the influence of the geometry and the material mismatch of the adhesive layer upon the response of the coupled structure is provided. Both edge and central debonding and their effect upon the stress distribution in the composite structure are discussed. The simulation results indicate that the increase of the bonding layer thickness will increase the shear stress distribution level along the internal of the actuator, and decrease the strain concentration at the tips of the actuator. Besides, the material combination of the actuator and the host structure needs to be carefully selected in order to improve actuator efficiency.

Chapter 4

Analysis of the Piezoelectric Sensor System

4.1 Introduction

The objective of this chapter is to provide a comprehensive theoretical study of the effect of imperfect bonding on the electromechanical behaviour of surface-bonded piezoelectric sensors. The current work is an extension of the work presented in Ref. [85] in which an integrated model containing a piezoelectric thin-sheet sensor, a viscoelastic bonding layer and an elastic medium (host) is proposed to evaluate its dynamic property under different loading frequencies. Although the effect of the geometrical and material property of the system has been investigated intensively, less effort has been devoted to the study of the debonded sensors. In this chapter, we focus on the effect of interfacial debonding in the static case where the loading frequency is so low that the typical wavelength of the incident wave is much longer than the length of the sensor. The imperfect bonding and its effect upon the strain distribution and the overall performance of the structure are evaluated in detail. Numerical simulation is conducted to simulate the effect of the geometrical and material property of the system, especially that of the imperfect bonding layer upon the coupled response of the sensors.

4.2 Formulation of the Problem

Let us now consider the plane strain problem of a thin piezoceramic sensor sheet bonded to a homogeneous and isotropic elastic half plane through a thin bonding layer, as illustrated in Fig. 3.1. The host medium is modelled as a half plane to represent the case that it is much thicker than the sensor. The lengths of both the sensor and the bonding layer are denoted as $2a$, and the thicknesses of the sensor and the bonding layer are denoted as h and h', respectively. It is assumed that the poling direction of the sensor is along the z-axis. Throughout this chapter superscripts s, b and h are used to designate physical quantities that belong to the sensor, the bonding layer and the host, respectively.

4.2.1 The sensor

This study will focus on a thin-sheet sensor, with relatively small thickness in comparison with its length. Therefore, the axial stress and strain can be assumed to be uniform across the thickness of the sensor. Since the thickness of the bonding layer is usually smaller than that of the sensor, the same assumption is also used for the bonding layer. The interfacial shear stress distributed between different layers, and the longitudinal displacements on the upper and lower surface of the bonding layer are shown in Fig. 3.1.

Based upon these assumptions, the sensor can be modelled as an electroelastic line subjected to the distributed axial force, τ/h. The equilibrium equation of the sensor can then be expressed as

$$\frac{d\sigma_y^s(y)}{dy} + \frac{\tau(y)}{h} = 0 \tag{4.1}$$

The electromechanical behaviour of the piezoelectric sensor can be described by

$$\sigma_y^s = E^s \epsilon_y^s - e^s E_z, \quad D_z = e^s \epsilon_y^s + \lambda^s E_z \tag{4.2}$$

where λ^s, E^s and e^s are effective material constants. D_z and E_z represent the electric displacement and the electric field intensity, respectively.

Since all the load transferred between the sensor and the bonding layer can be attributed to τ, the two ends of the sensor can be assumed to be traction free, i.e. $\sigma_y^s = 0$ at $|y| = a$. In addition, the sensor will be assumed to operate in an open-loop mode with no external charge supplied to it [90]. Therefore, the electric displacement across the sensor will be zero, i.e. $D_z = 0$.

The resulting axial strain ϵ_y^s and displacement u_y^s can then be expressed in terms of τ as

$$\epsilon_y^s(y) = -\frac{1}{\overline{E}^s h}\int_{-a}^{y} \tau(\xi)d\xi, \quad u_y^s(y) = -\frac{1}{\overline{E}^s h}\int_{-a}^{y} (y-\xi)\tau(\xi)d\xi, \quad |y| < a \tag{4.3}$$

where $\overline{E}^s = E^s + (e^s)^2/\lambda^s$.

4.2.2 The bonding layer

The bonding layer is the medium between the sensor and the host structure. Its shear modulus, thickness, and coefficient of viscosity, will govern the property of the layer. The shear stress τ distributed in the layer is determined by the constitutive relation:

$$-\tau(y) = \mu^b \varepsilon_y^b(y) \tag{4.4}$$

where

$$\varepsilon_y^b(y) = \frac{u^+(y) - u^-(y)}{h'} \tag{4.5}$$

with μ^b and ε_y^b being the shear modulus and the shear strain of the bonding layer, respectively. u^+ and u^- represent the longitudinal displacements of the lower surface of the sensor and the upper surface of the host medium, respectively.

4.2.3 The host medium

The stress field generated inside the host medium can be divided into two parts [85]. The first is caused by the incident wave in the host medium with a traction free boundary and the second is caused by surface shear stress τ resulted from the sensor. For the second subproblem, the displacement induced by τ can be determined by using the boundary condition along the top surface, which can be expressed as

$$\sigma_{yz}(y,0) = \begin{cases} -\tau(y) & |y| < a \\ 0 & |y| > a \end{cases}, \quad \sigma_z(y,0) = 0 \tag{4.6}$$

Making use of the fundamental solution of a half elastic plane subjected to a concentrated horizontal force [87] and the superposition principle, ϵ_y^h and u_y^h resulting from the applied force given by Eq. (4.6) can be obtained.

For the static case where a constant strain ϵ_y^{IN} is applied along the y-direction at infinity, the total strain and displacement can then be obtained by superimposing the solutions of both parts, which can be expressed as

$$\epsilon_y^h(y,0) = \frac{1-\nu^h}{\pi\mu^h}\int_{-a}^{a}\frac{\tau(\xi)}{y-\xi}d\xi + \epsilon_y^{IN}, \quad |y| < a \tag{4.7}$$

$$u_y^h(y,0) = \frac{1-\nu^h}{\pi\mu^h}\int_{-a}^{y}\int_{-a}^{a}\frac{\tau(\xi)}{y-\xi}d\xi dy + u_y^{IN}, \quad |y| < a \tag{4.8}$$

where ν^h and μ^h are the Poisson's ratio and the shear modulus of the host,

respectively.

4.2.4 Static load transfer in a perfectly bonded piezoelectric sensor

Substituting Eqs. (4.3) and (4.7) into Eq. (4.4), the following integral equation can be obtained

$$\left.\begin{aligned} \frac{1-\nu^h}{\pi\mu^h}\int_{-a}^{a}\frac{\tau(\xi)}{y-\xi}d\xi+\frac{1}{h\overline{E}^s}\int_{-a}^{y}\tau(\xi)d\xi-\frac{h'}{\mu^b}\frac{d\tau(y)}{dy}=-\epsilon_y^{IN}, \quad |y|<a \\ \int_{-a}^{a}\tau(\xi)d\xi=0 \end{aligned}\right\} \tag{4.9}$$

which can be normalized as

$$\left.\begin{aligned} \frac{1}{q}\int_{-1}^{1}\frac{\overline{\tau}(\zeta)d\zeta}{\eta-\zeta}+\frac{1}{v}\int_{-1}^{\eta}\overline{\tau}(\zeta)d\zeta-\frac{v'}{q'}\frac{d\overline{\tau}(\eta)}{d\eta}=-\epsilon_y^{IN}, \quad |\eta|<1 \\ \int_{-1}^{1}\overline{\tau}(\zeta)d\zeta=0 \end{aligned}\right\} \tag{4.10}$$

where

$$\overline{\tau}(\eta)=\frac{\tau(a\eta)}{\overline{E}^s},\ \eta=\frac{y}{a},\ q=\frac{\pi E^h}{2[1-(\nu^h)^2]\overline{E}^s},\ v=\frac{h}{a},\ q'=\frac{\mu^b}{\overline{E}^s},\ v'=\frac{h'}{a} \tag{4.11}$$

The general solutions of $\overline{\tau}$ in Eq. (4.10) can be expressed in terms of the following expansions of Chebyshev polynomials

$$\overline{\tau}(\eta)=\frac{1}{\sqrt{1-\eta^2}}\sum_{j=0}^{\infty}d_jT_j(\eta) \tag{4.12}$$

By truncating the Chebyshev polynomial expansions to the Nth term and considering the boundary conditions at the following collocation points along the sensor

$$\eta_k=\cos\left(\frac{k}{N+1}\pi\right), \quad k=1,2,\cdots,N \tag{4.13}$$

Eq. (4.10) reduces to

$$\sum_{j=1}^{N} d_j \frac{\sin\left(j\frac{k}{N+1}\pi\right)}{\sin\left(\frac{k}{N+1}\pi\right)}\left\{\frac{1}{q}+\frac{1}{v\pi j}\sin\left(\frac{k}{N+1}\pi\right)\right.$$
$$\left.+\frac{v'}{\pi q'}\left[\frac{j+\cot\left(j\frac{k}{N+1}\pi\right)\cot\left(\frac{k}{N+1}\pi\right)}{\sin\left(\frac{k}{N+1}\pi\right)}\right]\right\}=\frac{\epsilon_y^{IN}}{\pi},\quad k=1,2,\cdots,N \tag{4.14}$$

The unknown coefficients d_j can be readily determined by using Eq. (4.14). It can then be used to determine the axial displacement and the axial strain of the sensor.

4.2.5 Effect of interfacial debonding

The high level of shear stress at the edges of the sensor may result in an unwanted edge debonding as shown in Fig. 3.2. For a perfectly bonded sensor, when the maximum shear stress is larger than the bonding strength, edge debonding may develop. The debonded part of the sensor has zero boundary stresses. According to the present sensor model, the debonded part at the edge of the sensor will experience no stress. As a result, the effective length of the sensor is reduced from its original length to that of the bonded part only. Therefore, the behaviour of an edge debonded sensor can be simulated by a shorter sensor.

Debonding may also occur in the interior of the sensor. Let us consider a sensor occupying the region $t_l < y < t_r$ which is partially debonded in $d_l < y < d_r$ as illustrated in Fig. 3.3. The partially debonded sensor can then be regarded as two "sensors" subjected to an axial stress σ_d at the inner tips

of them. The resulting axial strain can then be expressed in terms of τ as

$$\epsilon_y^s(y) = \begin{cases} -\dfrac{1}{\overline{\overline{E}}^s h}\displaystyle\int_{t_l}^{y} \tau(\xi)d\xi & t_l < y < d_l \\ \dfrac{\sigma_d}{\overline{\overline{E}}^s} & d_l < y < d_r \\ \dfrac{1}{\overline{\overline{E}}^s h}\Big[\sigma_d h - \displaystyle\int_{d_r}^{y} \tau(\xi)d\xi\Big] & d_r < y < t_r \end{cases} \tag{4.15}$$

where

$$\sigma_d = -\int_{t_l}^{d_l} \frac{\tau(\xi)}{h} d\xi \tag{4.16}$$

The half plane to which the sensor is bonded is subjected to the following boundary conditions:

$$\sigma_{yz}(y,0) = \begin{cases} -\tau(y) & t_l < y < d_l \ \text{ and } \ d_r < y < t_r \\ 0 & \text{otherwise} \end{cases} \tag{4.17}$$

The surface strain in the host medium can be obtained by making use of the fundamental solution of a half plane subjected to a concentrated surface force. For the case where a constant strain ϵ_y^{IN} is applied along the y-direction at infinity, the total strain and displacement can then be obtained by superimposing the solutions of both parts, which can be expressed as

$$\epsilon_y^h(y,0) = \frac{1-\nu^h}{\pi\mu^h}\Big[\int_{t_l}^{d_l} \frac{\tau(\xi)}{y-\xi} d\xi + \int_{d_r}^{t_r} \frac{\tau(\xi)}{y-\xi} d\xi\Big] + \epsilon_y^{IN} \tag{4.18}$$

The strains in the sensor and the host medium presented by Eqs. (4.15)

and (4.18) can be related as

$$\begin{aligned}
&\frac{1-\nu^h}{\pi\mu^h}\int_{t_l}^{d_l}\frac{\tau(\xi)}{y-\xi}d\xi+\frac{1-\nu^h}{\pi\mu^h}\int_{d_r}^{t_r}\frac{\tau(\xi)}{y-\xi}d\xi-\frac{h'}{\mu^b}\frac{d\tau(y)}{dy}\\
&+\begin{cases}\dfrac{1}{h\overline{\overline{E}}^s}\displaystyle\int_{t_l}^{y}\tau(\xi)d\xi=-\epsilon_y^{IN} & t_l<y<d_l\\ \\ \dfrac{1}{h\overline{\overline{E}}^s}\displaystyle\int_{d_r}^{y}\tau(\xi)d\xi=\dfrac{\sigma_d}{\overline{\overline{E}}^s}-\epsilon_y^{IN} & d_r<y<t_r\end{cases}
\end{aligned}\tag{4.19}$$

The axial stress σ_d in Eq. (4.19) need to be determined by considering the deformation of the debonded part of the sensor. From Eqs. (4.4) and (4.5) it can be obtained that

$$u_y^s(d_r)-u_y^s(d_l)=u_y^h(d_r)-u_y^h(d_l)+\frac{h'}{\mu^b}[\tau(d_l)-\tau(d_r)]\tag{4.20}$$

Integrating Eqs. (4.15) and (4.18) and making use of Eq. (4.20) give the following equation, which provides an additional condition for determining σ_d

$$\begin{aligned}
\frac{1-\nu^h}{\pi\mu^h}\int_{d_l}^{d_r}\Big[\int_{t_l}^{d_l}\frac{\tau(\xi)}{y-\xi}d\xi+\int_{d_r}^{t_r}\frac{\tau(\xi)}{y-\xi}d\xi\Big]dy+\frac{h'}{\mu^b}[\tau(d_l)-\tau(d_r)]\\
=\Big(\frac{\sigma_d}{\overline{\overline{E}}^s}-\epsilon_y^{IN}\Big)(d_r-d_l)
\end{aligned}\tag{4.21}$$

Eqs. (4.16), (4.19) and (4.21) can be normalized as

$$\begin{aligned}
&\frac{1}{q}\int_{-1}^{1}\frac{\tau^l(\zeta)d\zeta}{\eta_l-\zeta}+\frac{1}{q}\int_{-1}^{1}\frac{\tau^r(\zeta)d\zeta}{\eta_r-\zeta}\\
&+\begin{cases}-\dfrac{v_l'}{q'}\dfrac{d\tau^l(\eta_l)}{d\eta_l}+\dfrac{1}{v_l}\displaystyle\int_{-1}^{\eta_l}\tau^l(\zeta)d\zeta=-\epsilon_y^{IN} & |\eta_l|<1\\ -\dfrac{v_r'}{q'}\dfrac{d\tau^r(\eta_r)}{d\eta_r}-\dfrac{1}{v_r}\displaystyle\int_{\eta_r}^{1}\tau^r(\zeta)d\zeta=-\epsilon_y^{IN} & |\eta_r|<1\end{cases}
\end{aligned}\tag{4.22}$$

$$\frac{1}{v_l}\int_1^{\eta_l^*}\int_{-1}^{1}\frac{\tau^l(\zeta)d\zeta}{\eta_l-\zeta}d\eta_l+\frac{1}{v_r}\int_{\eta_r^*}^{-1}\int_{-1}^{1}\frac{\tau^r(\zeta)d\zeta}{\eta_r-\zeta}d\eta_r+\frac{qv_l'}{q'v_l}\tau^l(1)-\frac{qv_r'}{q'v_r}\tau^r(-1)$$
$$=2q\Big(\frac{1}{v}-\frac{1}{v_l}-\frac{1}{v_r}\Big)(\sigma^*-\epsilon_y^{IN}) \tag{4.23}$$

and

$$\int_{-1}^{1}\tau^l(\zeta)d\zeta=-\sigma^*v_l,\quad \int_{-1}^{1}\tau^r(\zeta)d\zeta=\sigma^*v_r \tag{4.24}$$

where the normalized stresses are given by

$$\tau^l(\eta_l)=\frac{\tau(a_l\eta_l+y_l)}{\overline{\overline{E}}^s},\quad \tau^r(\eta_r)=\frac{\tau(a_r\eta_r+y_r)}{\overline{\overline{E}}^s},\quad \sigma^*=\frac{\sigma_d}{\overline{\overline{E}}^s} \tag{4.25}$$

with

$$\left.\begin{gathered}\eta_l=\frac{y-y_l}{a_l},\quad \eta_r=\frac{y-y_r}{a_r}\\ v=\frac{h}{a},\ v_l=\frac{h}{a_l},\ v_r=\frac{h}{a_r}\\ v'=\frac{h'}{a},\ v_l'=\frac{h'}{a_l},\ v_r'=\frac{h'}{a_r}\\ a=\frac{1}{2}(t_r-t_l),\ a_l=\frac{1}{2}(d_l-t_l),\ a_r=\frac{1}{2}(t_r-d_r)\\ y_l=\frac{1}{2}(d_l+t_l),\ y_r=\frac{1}{2}(t_r+d_r)\\ \eta_l^*=2v_l\frac{v_r-v}{v_rv}-1,\quad \eta_r^*=-2v_r\frac{v_l-v}{v_lv}+1\end{gathered}\right\} \tag{4.26}$$

The general solutions of τ^l and τ^r in Eqs. (4.22)–(4.24) can then be expressed in terms of the following expansions of Chebyshev polynomials

$$\tau^l(\eta_l)=\frac{1}{\sqrt{1-\eta_l^2}}\sum_{j=0}^{\infty}d_j^lT_j(\eta_l),\quad \tau^r(\eta_r)=\frac{1}{\sqrt{1-\eta_r^2}}\sum_{j=0}^{\infty}d_j^rT_j(\eta_r) \tag{4.27}$$

If the Chebyshev polynomial expansions are truncated to the Nth term, and Eq. (4.22) is satisfied at the following collocation points at each bonded

segment of the sensor given by

$$\eta_{lk} = \eta_{rk} = \eta_k = \cos\Big(\frac{k}{N+1}\pi\Big), \quad k = 1, 2, \cdots, N \tag{4.28}$$

Eqs. (4.22) and (4.23) reduce to

$$\begin{aligned}
&\sum_{j=1}^{N} d_j^l \frac{\sin\Big(j\frac{k}{N+1}\pi\Big)}{\sin\Big(\frac{k}{N+1}\pi\Big)}\Bigg\{\frac{1}{q} + \frac{1}{v_l \pi j}\sin\Big(\frac{k}{N+1}\pi\Big) \\
&\qquad + \frac{v_l'}{\pi q'}\left[\frac{j + \cot\Big(j\frac{k}{N+1}\pi\Big)\cot\Big(\frac{k}{N+1}\pi\Big)}{\sin\Big(\frac{k}{N+1}\pi\Big)}\right]\Bigg\} \\
&+\sum_{j=1}^{N} d_j^r \frac{\Big[\sqrt{(\eta_{rk}')^2 - 1} - |\eta_{rk}'|\Big]^j}{q\sqrt{(\eta_{rk}')^2 - 1}} + \frac{\sigma^*}{\pi}\left[\frac{v_r}{q\sqrt{(\eta_{rk}')^2 - 1}} + \Big(1 - \frac{k}{N+1}\Big)\right. \\
&\qquad \left. - \frac{v_l' v_l}{\pi q'}\frac{\cot\Big(\frac{k}{N+1}\pi\Big)}{\sin^2\Big(\frac{k}{N+1}\pi\Big)}\right] = \frac{\epsilon_y^{IN}}{\pi}, \quad k = 1, 2, \cdots, N
\end{aligned} \tag{4.29}$$

$$\begin{aligned}
&\sum_{j=1}^{N} d_j^r \frac{\sin\Big(j\frac{k}{N+1}\pi\Big)}{\sin\Big(\frac{k}{N+1}\pi\Big)}\Bigg\{\frac{1}{q} + \frac{1}{v_r \pi j}\sin\Big(\frac{k}{N+1}\pi\Big) \\
&\qquad + \frac{v_r'}{\pi q'}\left[\frac{j + \cot\Big(j\frac{k}{N+1}\pi\Big)\cot\Big(\frac{k}{N+1}\pi\Big)}{\sin\Big(\frac{k}{N+1}\pi\Big)}\right]\Bigg\} \\
&-\sum_{j=1}^{N} d_j^l (-1)^j \frac{\Big[\sqrt{(\eta_{lk}')^2 - 1} - |\eta_{lk}'|\Big]^j}{q\sqrt{(\eta_{lk}')^2 - 1}} + \frac{\sigma^*}{\pi}\left[\frac{v_l}{q\sqrt{(\eta_{lk}')^2 - 1}} + \frac{k}{N+1}\right. \\
&\qquad \left. + \frac{v_r' v_r}{\pi q'}\frac{\cot\Big(\frac{k}{N+1}\pi\Big)}{\sin^2\Big(\frac{k}{N+1}\pi\Big)}\right] = \frac{\epsilon_y^{IN}}{\pi}, \quad k = 1, 2, \cdots, N
\end{aligned} \tag{4.30}$$

$$
\begin{aligned}
&-\sigma^*\Bigg[\frac{1}{q}\ln|\eta_l^*+\sqrt{\eta_l^{*2}-1}|-\frac{1}{q}\ln|\eta_r^*+\sqrt{\eta_r^{*2}-1}| \\
&\qquad +2\Big(\frac{1}{v}-\frac{1}{v_l}-\frac{1}{v_r}\Big)+\frac{v_r'+v_l'}{\pi q'\sin\Big(\dfrac{1}{N+1}\pi\Big)}\Bigg] \\
&+\sum_{j=1}^{N}\frac{d_j^l}{v_l}\Bigg\{\pi(-1)^j\int_1^{\eta_l^*}\frac{\Big[\sqrt{(\eta_{lk}')^2-1}-|\eta_{lk}'|\Big]^j}{q\sqrt{(\eta_{lk}')^2-1}}d\eta_{lk}'+\frac{v_l'}{q'}\frac{\cos\Big(j\dfrac{1}{N+1}\pi\Big)}{\sin\Big(\dfrac{1}{N+1}\pi\Big)}\Bigg\} \\
&+\sum_{j=1}^{N}\frac{d_j^r}{v_r}\Bigg\{-\pi\int_{\eta_r^*}^{-1}\frac{\Big[\sqrt{(\eta_{rk}')^2-1}-|\eta_{rk}'|\Big]^j}{q\sqrt{(\eta_{rk}')^2-1}}d\eta_{rk}'-(-1)^j\frac{v_r'}{q'}\frac{\cos\Big(j\dfrac{1}{N+1}\pi\Big)}{\sin\Big(\dfrac{1}{N+1}\pi\Big)}\Bigg\} \\
&\qquad =-2\Big(\frac{1}{v}-\frac{1}{v_l}-\frac{1}{v_r}\Big)\epsilon_y^{IN} \qquad (4.31)
\end{aligned}
$$

where

$$\eta'_{lk}=v_l\Big[\frac{2}{v}-\frac{1}{v_l}-\frac{1}{v_r}+\frac{1}{v_r}\cos\Big(\frac{k}{N+1}\pi\Big)\Big] \qquad (4.32)$$

$$\eta'_{rk}=-v_r\Big[\frac{2}{v}-\frac{1}{v_l}-\frac{1}{v_r}-\frac{1}{v_l}\cos\Big(\frac{k}{N+1}\pi\Big)\Big] \qquad (4.33)$$

The unknown coefficients d_j^l, d_j^r and σ^* can be determined by solving Eqs. (4.29)–(4.31), which can then be used to determine the axial displacement and the axial strain of the debonded sensor.

4.3 Numerical Results and Discussion

In this section, the results of numerical simulation of the influence of the property of the bonding layer under different material combinations and sensor geometries on the electromechanical behaviour of the integrated system are presented. The attention will be focused on the strain distribution along the

Table 4.1: Material Properties of the Host Medium and the Bonding Layer

Host medium	
Young's modulus E^h (Pa)	2.74×10^{10}
Poisson's ratio ν^h	0.3
Bonding layer	
Shear modulus μ^b (Pa)	1.0×10^9

sensor, which represents the load transfer between the sensor and the host medium. The convergence of the solution using Chebyshev polynomials has been carefully evaluated. The number of terms of Chebyshev polynomials is selected to be 64, with which the convergence of the results for all the cases considered is ensured.

The piezoelectric material considered in the following examples is a typical piezoceramics, whose properties are given in Table 3.1 [88]. The properties of the bonding layer [7] and the host medium [89] are given in Table 4.1. From these material constants it can be determined that $q = 0.3928$ and $q' = 0.0083$. The geometry of the sensor is assumed to be $a = 1.0$ cm and $h = 500$–2000 μm. The length of the bonding layer is the same as that of the sensor.

4.3.1 Sensor with a uniform interfacial layer

4.3.1.1 Strain distribution along the sensor

The relation between the sensor strain ϵ_y^s and the strain to be measured ϵ_y^{IN} can be evaluated using the amplitude of a static strain ratio, $\kappa(y)$, defined as

$$\kappa(y) = \frac{\epsilon_y^s(y)}{\epsilon_y^{IN}}, \quad |y/a| < 1 \tag{4.34}$$

which represents the percentage of deformation transferred from the host medium to the sensor. Ideally, if the sensor does not disturb the incident field the value should be one. The change of κ represents the intrusive effect of the sensor on the original incident field. As shown in Eq. (4.11), q represents the material combination of the sensor and the host structure, v represents sensor geometry, q' represents material property of the bonding layer and v' represents the geometry of the bonding layer. Carefully examining Eq. (4.10) indicates that the strain distribution is governed by three parameters: q, v and v'/q'. In the following discussion, the values of q, v and v' are varied to evaluate different responses of the structure.

Fig. 4.1 shows the effect of $v = h/a$ upon the amplitude of the strain ratio $A = |\kappa(y)|$ along the sensor with $q = 0.3928$ and $v' = 0$. Significant effect of v upon the strain ratio is observed, with lower value of v corresponding to relatively higher strain ratio, indicating that sensors with higher length-to-thickness ratio have a higher sensitivity. To validate the model, a numerical analysis using commercially available finite element software ANSYS is conducted. Both the sensor and the host medium are modelled using PLANE13 elements, which can simulate coupled electromechanical fields. A comparison of the result from the current model with that of the finite element simulation is also made in Fig. 4.1. Excellent agreement is observed for $v = 0.05$, showing the feasibility and accuracy of the proposed sensor model. The corresponding result for the case where the bonding condition is $v' = 0.015$ is shown in Fig. 4.2. Again, significant effect of v is observed. In comparison with the results shown in Fig. 4.1, the strain transfer ratio is much lower for a given v especially near the ends of the sensor.

To study the effect of material mismatch q, the material constants of the

sensor are fixed, and the shear modulus of the host medium is changed to achieve different material combinations. For the convenience of calculation, $q = 0.2$, 0.5, 1.0, 2.0, 5.0 and 10.0, are chosen, and two bonding conditions, $v' = 0$ and $v' = 0.01$, are considered to investigate the effect of the material combination on the load transfer between the sensor and the host structure. Fig. 4.3 shows the strain distribution along the sensor for different q values when $v' = 0$. With the decrease of the stiffness of the sensor (increasing q), the amplitude of the normalized strain increases. When q reaches 5.0, the strain distribution curve becomes very flat, approaching 1.0 in most part of the sensor. This is because the disturbance of a soft sensor is relatively insignificant. It can be observed that when $q > 5.0$, the strain of the sensor provides a good prediction of the applied strain to be measured. For $q < 5.0$, however, significant difference between them is observed. We might as well consider two extreme cases where the sensor is either very stiff or very soft compared with the host medium. For a stiff sensor ($q \to 0$, $q/v \to 0$ is actually needed), the governing equation for the interfacial shear stress, Eq. (4.9) reduces to

$$\frac{1-\nu^h}{\pi\mu^h}\int_{-a}^{a}\frac{\tau(\xi)}{y-\xi}d\xi = -\epsilon_y^{IN}, \quad |y| < a \tag{4.35}$$

which can be solved analytically and results in the following strain ratio $\kappa(y) = q(1-\eta^2)^{1/2}/v$. In this case, the strain ratio will be very small but the distribution of it along the sensor can be predicted. When the sensor is very soft ($q \to \infty$), Eq. (4.9) reduces to

$$\frac{1}{h\overline{E}^s}\int_{-a}^{y}\tau(\xi)d\xi = -\epsilon_y^{IN}, \quad |y| < a \tag{4.36}$$

which results in $\kappa(y) = 1$. Theoretically, this is the perfect situation for

sensing. The corresponding result for the case where the bonding condition is $v' = 0.01$ is shown in Fig. 4.4. The strain distribution curves approach 1.0 only in the middle part of the sensor. This indicates that when the bonding layer is included, the disturbance of the sensor is significant even for large q.

Fig. 4.5 shows the amplitude of the strain ratio along the sensor for different bonding layer thickness $v' = 0$, 0.002, 0.004, 0.008 and 0.016 with $q = 0.3928$. A significant deduction of the strain ratio occurs with increasing bonding layer thickness. At $y/a = 0.75$ for example, a deduction of 20% of the strain ratio is observed when $v' = 0.008$ in comparison with the case $v' = 0$. The corresponding result for $q = 10.0$ is shown in Fig. 4.6. It is observed that the strain ratio is less than unity near the ends of the sensor. The length of this zone depends on v'/q', as shown in Eq. (4.10), which in turn depends on the stiffness and thickness of the bond layer. As μ^b increases and h' reduces, v'/q' reduces, and the deformation is effectively transferred even over very small zones near the ends of the sensor. Considering the fact that $q = 10.0$ corresponds to a very soft sensor, the current result indicates that, even when the host structure is much stiffer than the sensor, the effect of the bonding layer on the load transfer will still be very important.

4.3.1.2 Output voltage of the sensor

According to the relationship between voltage and electric field intensity, the voltage distribution along the sensor can be determined as

$$V(y) = -\int_0^h E_z(y)dz = \frac{e^s h}{\lambda^s}\frac{\partial u_y^s}{\partial y}. \tag{4.37}$$

When the upper and lower surfaces of the sensor form two electrodes, the total resulting voltage across the sensor can be obtained by averaging the voltage across the sensor obtained before, i.e.

$$V^{out} = \frac{1}{2a}\int_{-a}^{a} V(y)dy = \frac{e^s h}{2a\lambda^s}|u_y^s(a) - u_y^s(-a)|. \tag{4.38}$$

V^{out} is an important parameter of the piezoelectric sensor, which will be measured in a real system. The higher the V^{out} value, the stronger the signal detected by the sensor is.

Fig. 4.7 shows the variation of the normalized output voltage of the sensor with the thickness of the bonding layer and material combinations. The amplitude of the incident strain field is kept to be the same and the output voltage is normalized by $(V^{out})_0$, i.e. $B = |V^{out}/(V^{out})_0|$, where $(V^{out})_0$ is the corresponding result for $q = 10.0$ at $v' = 0$. It is shown that for a fixed value of q, the output voltage decreases with an increase in the thickness of the bonding layer; for a fixed value of v', the output voltage increases with increasing q. The increase of v', from 0.01 to 0.03 for example, will decrease the output voltage by up to 15.15% for $q = 0.2$ and 22.52% for $q = 10.0$, indicating that with the increase of q, the effect of the thickness of the bonding layer becomes more obvious.

Fig. 4.8 shows the variation of the normalized output voltage with the thickness of the bonding layer and sensor geometries. The output voltage is normalized by the corresponding result for $v = 0.2$ at $v' = 0$. It is shown that with a given v, the output voltage decreases with increasing v'; with a given v', the output voltage decreases with decreasing v.

4.3.2 Interfacial debonding

4.3.2.1 Edge debonding

For a perfectly bonded sensor, when the maximum shear stress is larger than the bonding strength, edge debonding will initiate and grow to a length d, as shown in Fig. 3.2. As mentioned in the last section, a debonded sensor can be regarded as a shorter sensor. The effective length of the sensor is reduced from its original length $2a$ to $2a_{eff} = 2a - d$.

To evaluate the effect of the thickness of the bonding layer in edge debonding problem, Fig. 4.9 shows the normalized output voltage as a function of d/a for $q = 0.3928$, $q' = 0.0083$ and $v = 0.05$. The output voltage is normalized by the corresponding result for $v' = 0$ at $d = 0$. As expected when the debonding continues developing, the output voltage decreases. It is also shown that the increase of the debonding length, from $d = 0$ to $d = a$ for example, will decrease the output voltage by up to 28.9% for $v' = 0.002$ and 42.4% for $v' = 0.016$, indicating that the effect of edge debonding becomes more significant with the increase of the thickness of the bonding layer.

4.3.2.2 Central debonding

Local stress concentration and/or weak interfacial bonding may also result in debonding in the interior of the sensor as shown in Fig. 3.3. To simulate this situation, the sensor considered is assumed symmetrically debonded in $|y| < d$, i.e. $t_r = -t_l = a$ and $d_r = -d_l = d$. The effective length of the sensor is reduced from its original length $2a$ to $2a_{eff} = 2(a - d)$.

Strain redistributions along sensors with central debondings for $q = 2.0$, $q' = 0.0083$ and $v = 0.05$ with two bonding conditions, $v' = 0$ and $v' = 0.01$,

are shown in Figs. 4.10 and 4.11, respectively. Fig. 4.10 shows that when the bonding layer is absent the central debonding shows insignificant effect on the load transfer between the debonded sensor and the host structure. It is also shown that central debondings mainly cause the strain redistribution in the debonding area, and does not significantly affect strain ratio far away from the debonding edge. However, when the bonding layer is included as illustrated in Fig. 4.11, the effect of debonding on the strain redistribution becomes much more obvious.

To investigate the effect of the material combination on the performance of the debonded sensor, the results for strain redistribution for $v = 0.05$, $q' = 0.0083$ and $d/a = 0.6$ under two bonding conditions, $v' = 0$ and $v' = 0.01$, are shown in Figs. 4.12 and 4.13, respectively. Fig. 4.12 shows that the central debonding has more effect on the strain redistribution for smaller q values. When a bonding layer is included, as shown in Fig. 4.13, the effect of debonding becomes significant for any value of q. It is also observed that the strain ratio along the undebonded part of the sensor is obviously increased.

The strain ratio along the debonded sensor for different bonding layer thickness for $q = 10.0$ is shown in Fig. 4.14. It is observed that even for a very soft sensor, the effect of central debonding will still be very important when the thickness of the bonding layer is significant.

To evaluate the variation of the output voltage of the sensor with the debonding length and the influence of different thicknesses of the bonding layers, Fig. 4.15 shows the normalized output voltage as a function of d/a for $q = 0.3928$, $q' = 0.0083$ and $v = 0.05$. The output voltage is normalized by the corresponding result for $v' = 0.001$ at $d = 0$. It is shown that the thickness of the bonding layer does show significant effect upon the normalized output

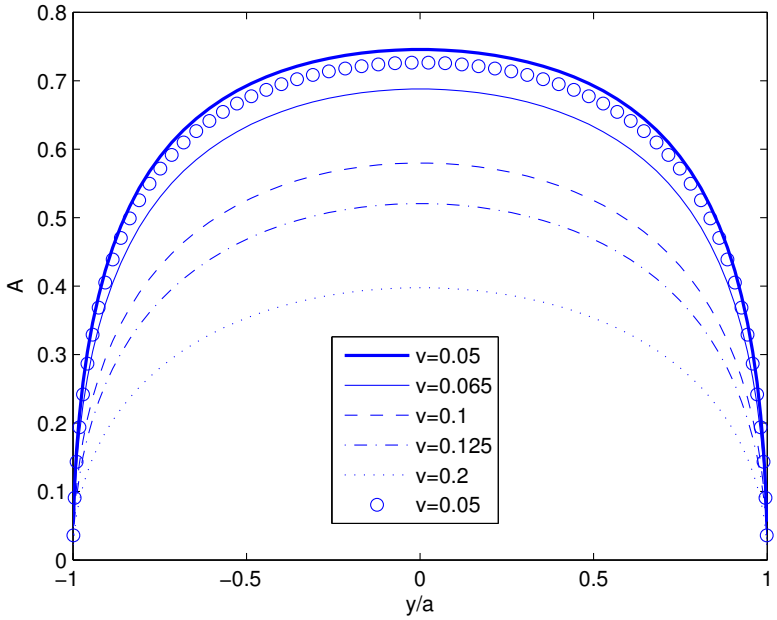

Figure 4.1: Amplitude of strain ratio ($q = 0.3928$ and $v' = 0$). Solutions obtained from current model are shown as lines and FEA as data points.

voltage. It should be mentioned, however, when the thickness of the layer is small compared with the thickness of the sensor, d/a shows insignificant effect until the debonding approaches the tip of the sensor.

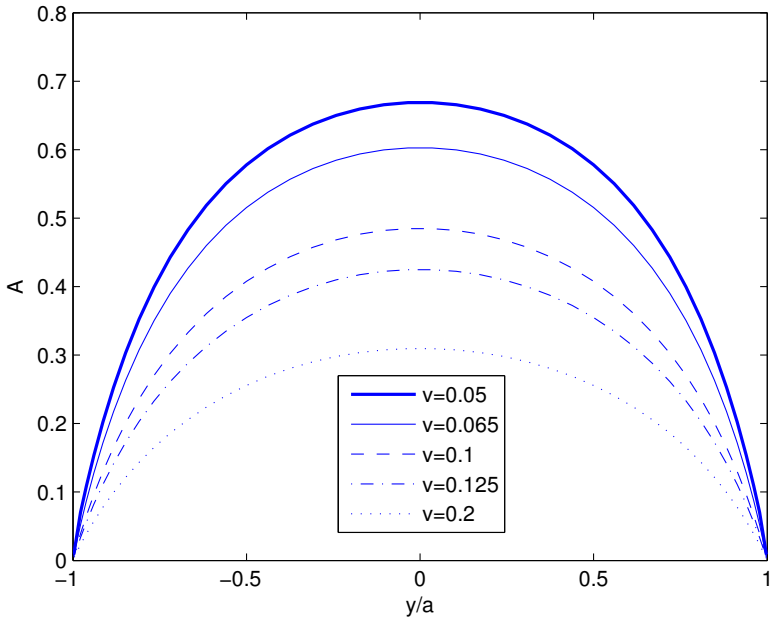

Figure 4.2: Amplitude of strain ratio ($q = 0.3928$, $q' = 0.0083$ and $v' = 0.015$).

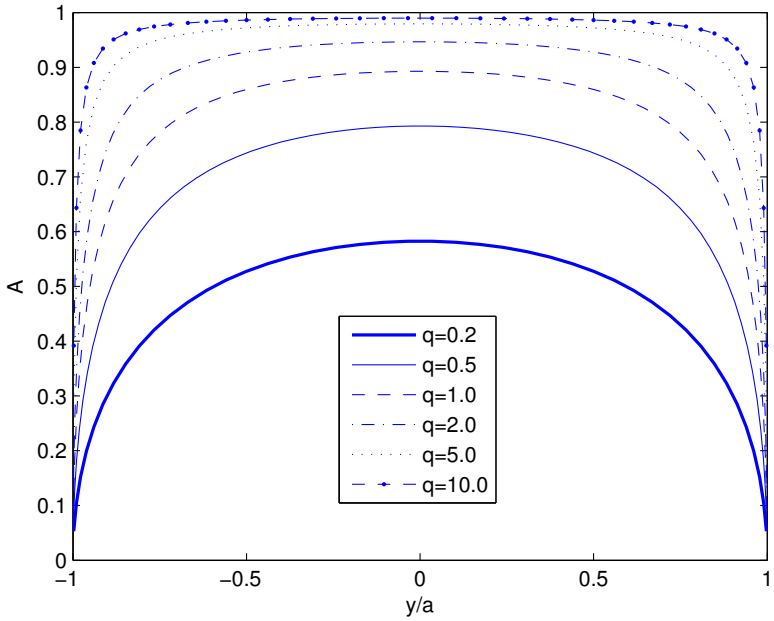

Figure 4.3: Amplitude of strain ratio ($v = 0.05$ and $v' = 0$).

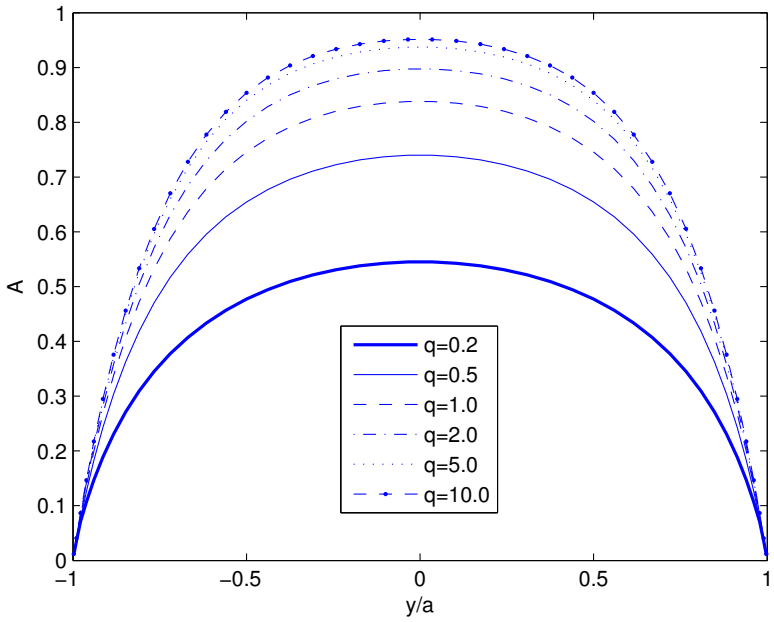

Figure 4.4: Amplitude of strain ratio ($v = 0.05$, $q' = 0.0083$ and $v' = 0.01$).

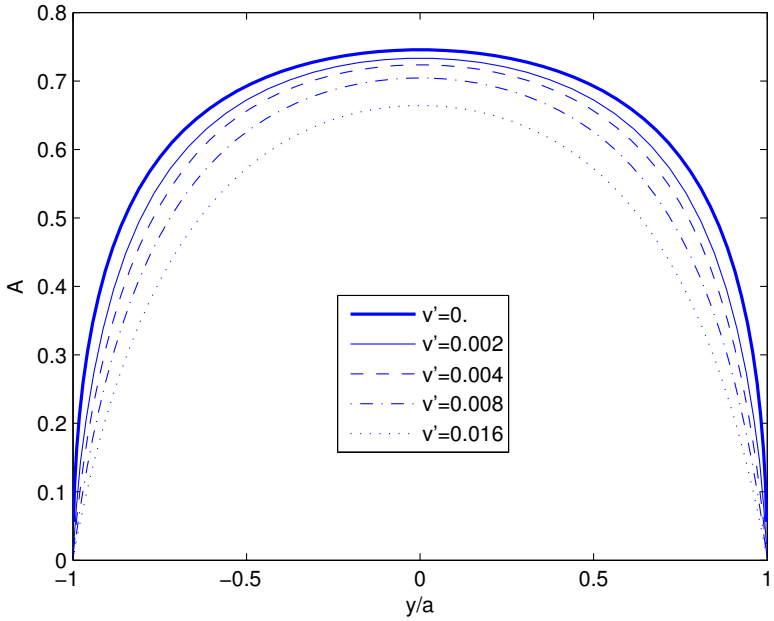

Figure 4.5: Amplitude of strain ratio ($q = 0.3928$, $q' = 0.0083$ and $v = 0.05$).

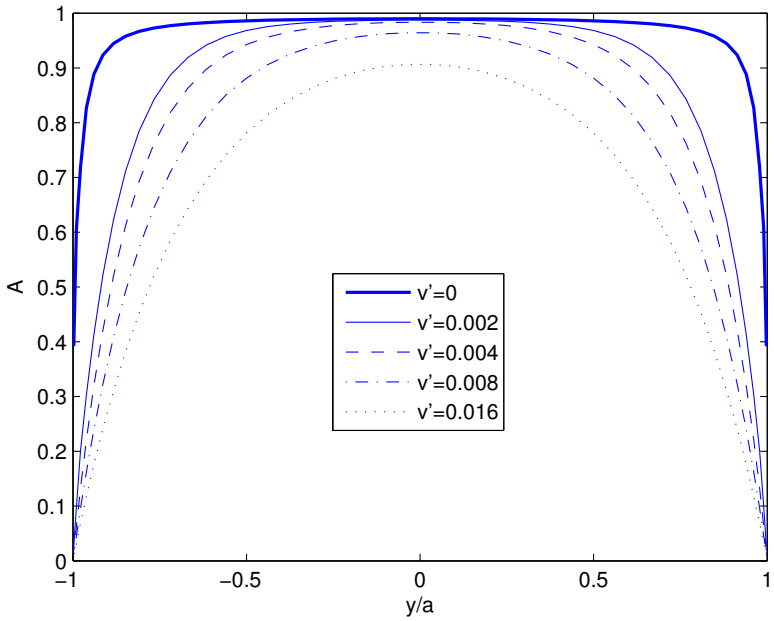

Figure 4.6: Amplitude of strain ratio ($q = 10.0$, $q' = 0.0083$ and $v = 0.05$).

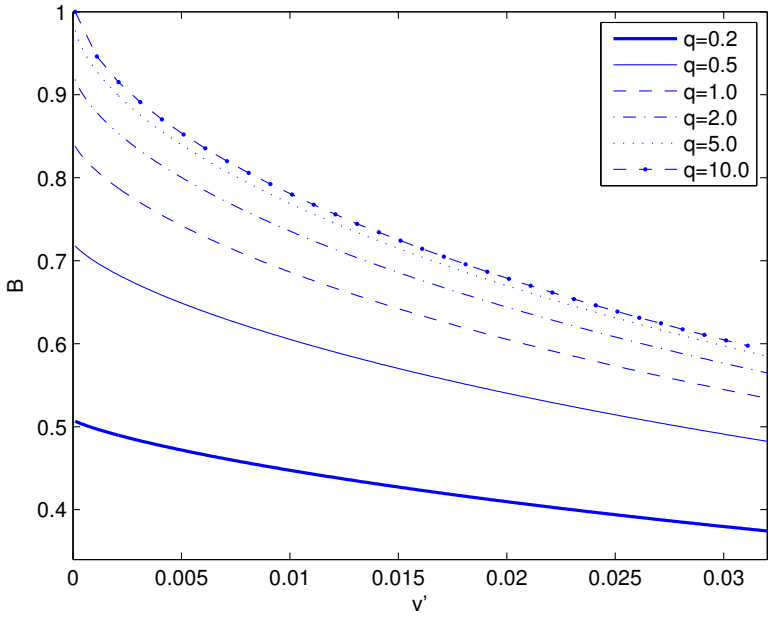

Figure 4.7: Normalized voltage distribution with different thicknesses of the bonding layer and material combinations ($q' = 0.0083$ and $v = 0.05$).

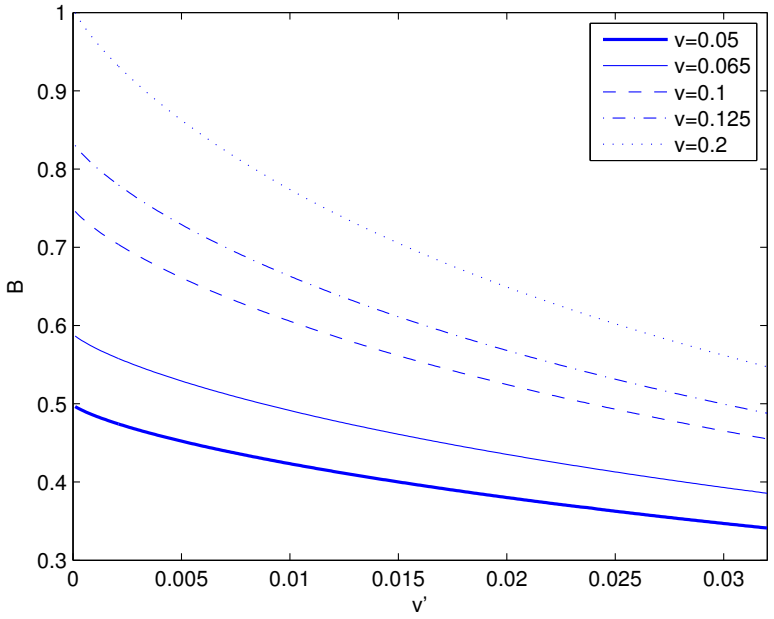

Figure 4.8: Normalized voltage distribution with different thicknesses of the bonding layer and sensor geometries ($q = 0.3928$ and $q' = 0.0083$).

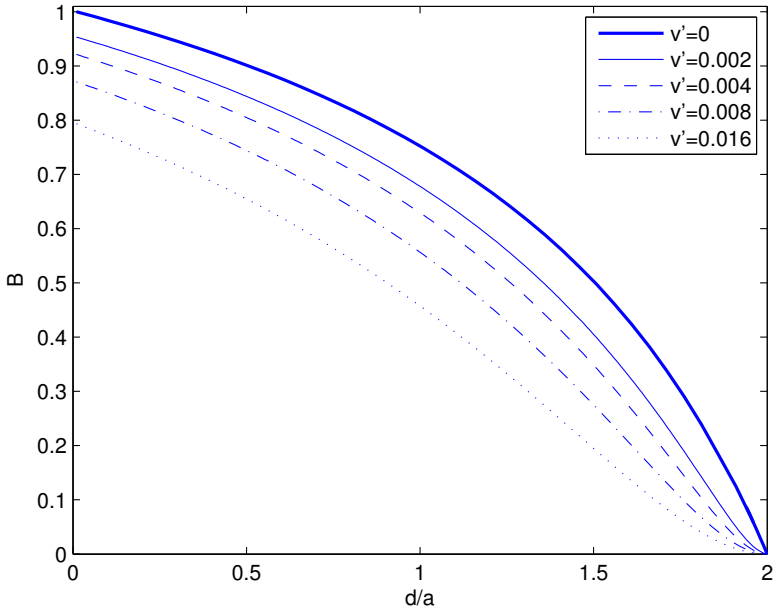

Figure 4.9: Normalized output voltage as a function of debonding length ($q = 0.3928$, $q' = 0.0083$ and $v = 0.05$).

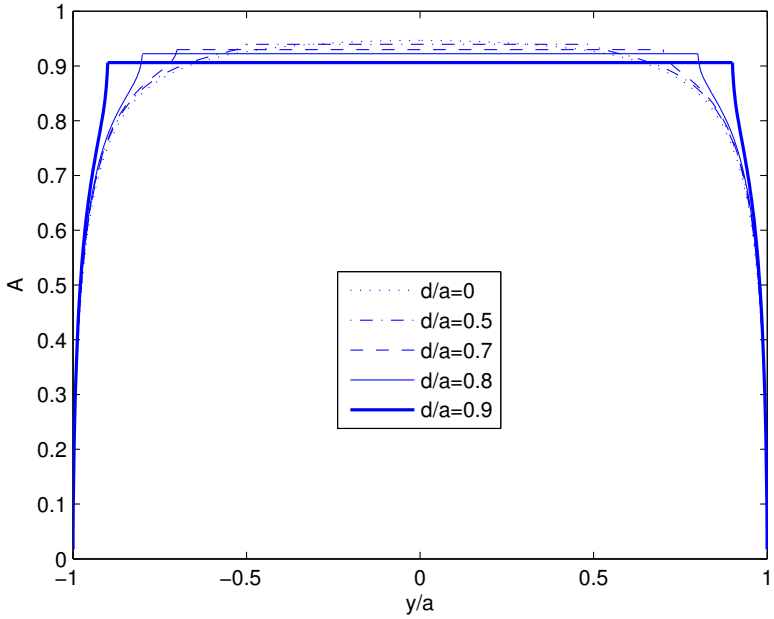

Figure 4.10: Amplitude of strain ratio ($q = 2.0$, $v = 0.05$ and $v' = 0$).

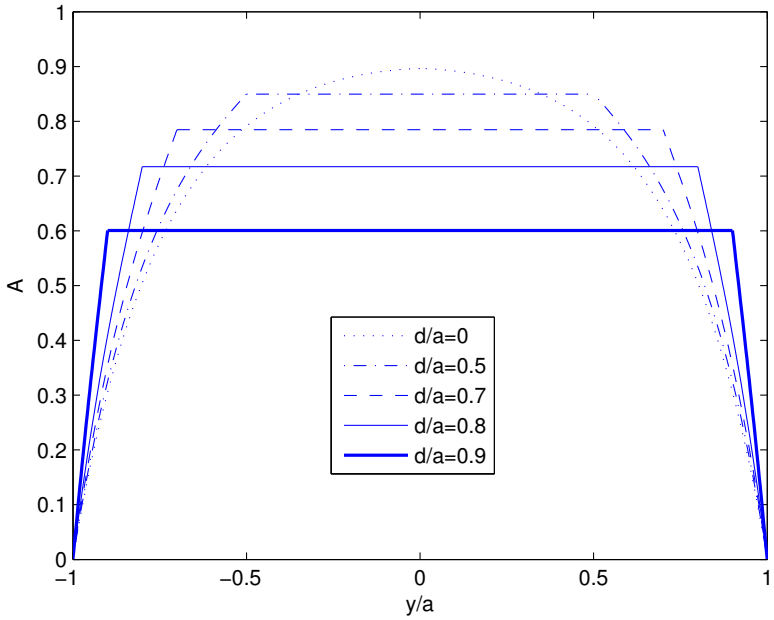

Figure 4.11: Amplitude of strain ratio ($q = 2.0$, $v = 0.05$, $q' = 0.0083$ and $v' = 0.01$).

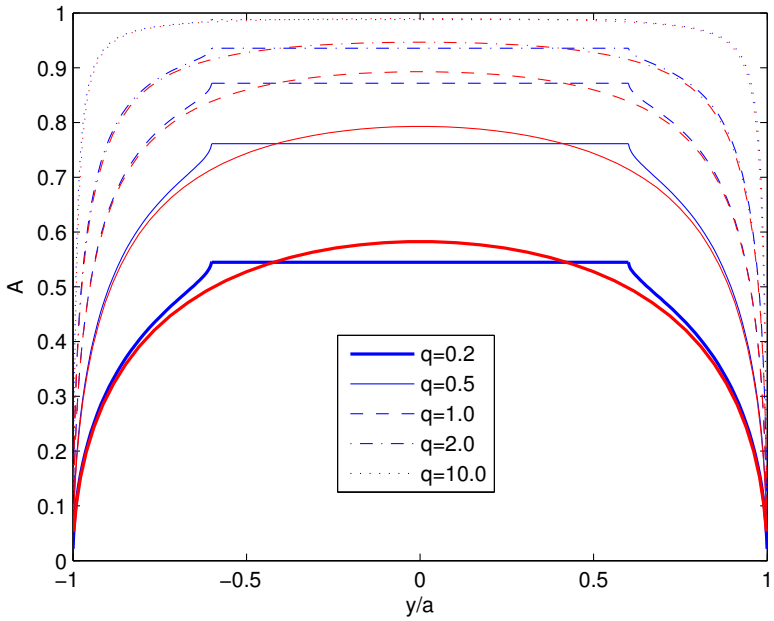

Figure 4.12: Amplitude of strain ratio ($v = 0.05$ and $v' = 0$). Red lines: undebonded cases ($d/a = 0$). Blue lines: debonded cases ($d/a = 0.6$).

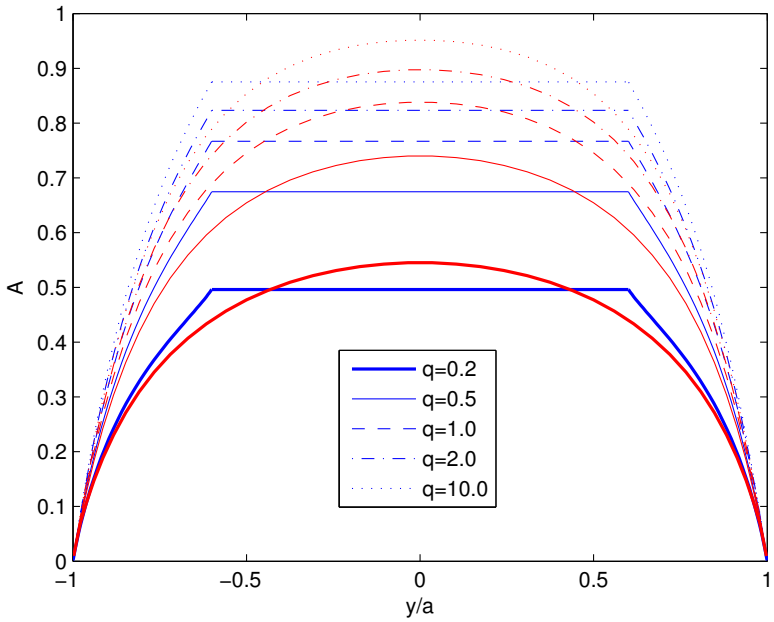

Figure 4.13: Amplitude of strain ratio ($v = 0.05$, $q' = 0.0083$ and $v' = 0.01$). Red lines: undebonded cases ($d/a = 0$). Blue lines: debonded cases ($d/a = 0.6$)

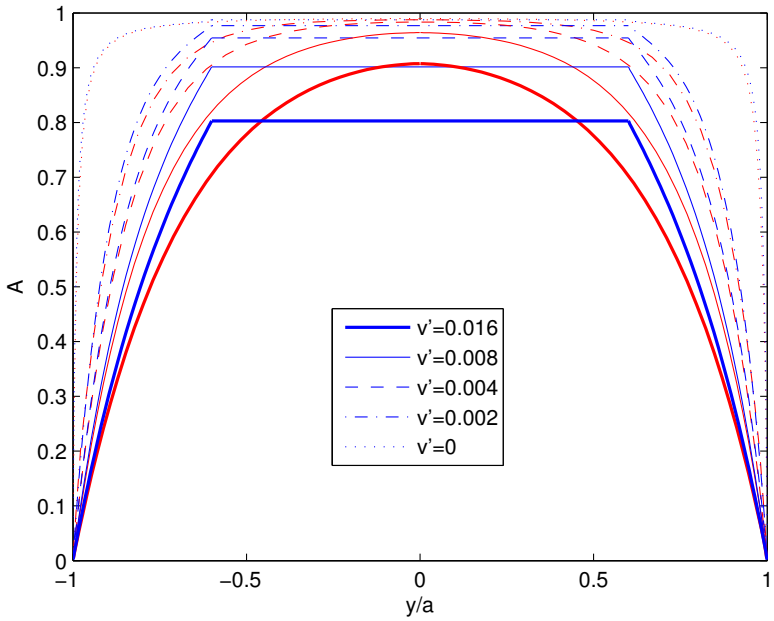

Figure 4.14: Amplitude of strain ratio ($q = 10.0$, $q' = 0.0083$ and $v = 0.05$). Red lines: undebonded cases ($d/a = 0$). Blue lines: debonded cases ($d/a = 0.6$).

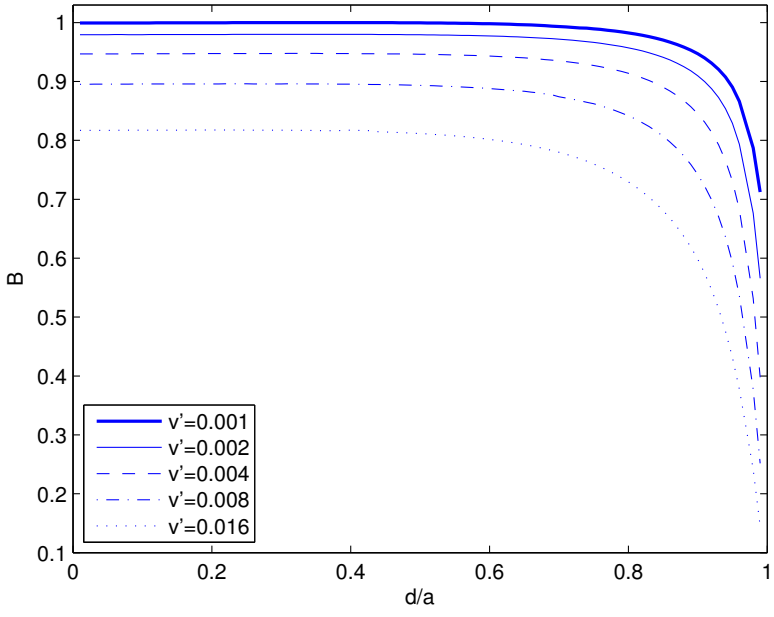

Figure 4.15: Normalized output voltage as a function of debonding length ($q = 0.3928$, $q' = 0.0083$ and $v = 0.05$).

4.4 Concluding Remarks

The focus of this chapter is on the study of the effect of the material and geometric properties of the sensor and the bonding layer on the load transfer from the sensor to the host medium. A general analytical solution is provided to the coupled electromechanical behaviour of a piezoelectric sensor bonded to a host through an adhesive bonding layer when the loading frequency is so low that the typical wavelength of the incident wave is much longer than the length of the sensor. The validity of the present model has been demonstrated by application to specific examples and comparison with the correspond results obtained from Finite Element method. The numerical investigation of the influence of the geometry and the material mismatch of the adhesive layer upon the response of the coupled structure is provided. Both edge and central debonding and their effect upon the strain distribution in the composite structure are discussed.

Chapter 5

Final Remarks

5.1 Contributions and Conclusions

The focus of this thesis is on the effect of the imperfect bonding layer on the static electromechanical behaviour of piezoelectric sensors and actuators. The current work is an extension of the work presented in Refs. [85,86] in which an integrated model containing a piezoelectric thin-sheet sensor/actuator, a viscoelastic bonding layer and an elastic medium (host) is proposed to evaluate its dynamic property under different loading frequencies. Although the effect of the geometrical and material property of the system has been investigated intensively, less effort has been devoted to the study of the debonding. In this thesis, we focus on the effect of interfacial debonding in the static case where the loading frequency is so low that the typical wavelength of the incident wave is much longer than the length of the sensor/actuator. The imperfect bonding and its effect upon the strain/stress distribution and the overall performance of the structure are evaluated in detail. Numerical simulation is conducted to simulate the effect of the geometrical and material property of the system, especially that of the imperfect bonding layer upon the coupled response of the sensors/actuators. Results indicate that with the decrease of the bonding layer

stiffness, the amplitude of the strain distribution along the sensor or the shear stress distribution along the actuator gets smaller, which corresponds to a decrease in sensor/actuator efficiency. Besides, with the existence of the bonding layer, the stress concentration at the tips of the sensor/actuator becomes less and less obvious, or even disappears, with the increase of the bonding layer thickness, which will reduce the chance of the sensor/actuator peeling off from the host structure. It is shown that it is important to take into account of the property of the bonding layer in order to select the optimal adhesive to minimize its effects.

Based on the analysis conducted in Chapter 3 and Chapter 4, the following specific conclusions, which are potentially useful in the design of piezoelectric sensors/actuators for SHM systems, can be obtained as follows:

(1) High stiffness of the bonding layer is preferred. This corresponds to thin bonding layer, or high layer modulus. However, since the strain concentration around the tips of the sensor/actuator increases as the bonding layer gets stiffer, attention should also be paid to make sure the sensor/actuator will not be peeling off from the host medium.

(2) The material combination of the sensor/actuator and the host structure needs to be carefully selected. Based on the current simulation, the material mismatch parameter q between 0.5 and 2.0 is an acceptable. If q is beyond this range, it will increase the effects of the bonding layer on the load transfer between the sensor/actuator and the host structure. In other words, significant difference of the load transfer can be observed between the cases when the bonding layer is included and is absent.

(3) In the edge debonding cases, when the debonding continues developing,

the edge stresses decrease. When the edge stresses decrease to the values below the interfacial toughness, the debonding will stop growing. This self-arresting mechanism becomes more obvious with the increase of the thickness of the bonding layer.

(4) Local stress concentration and/or weak interfacial bonding may also result in debonding in the interior of the actuator. The simulation result shows that when the bonding layer is ignored shear stresses concentrate near the debonding edge, particularly for larger debonding lengths; it may be detrimental to the bonding strength. It also shows that central debondings mainly cause the stress redistribution near the debonding area, and does not significantly affect stresses far away from the debonding. However, when the bonding layer is included shear stresses do not concentrate in the debonding edge and show a much more uniform distribution.

(5) The thickness of the bonding layer between the sensor and the host does show significant effect upon the normalized output voltage. It should be mentioned, however, when the thickness of the layer is small compared with the thickness of the sensor, the debonding length shows insignificant effect until the debonding approaches the tip of the sensor.

5.2 Future Work

The objective of this thesis is to study the effect of the bonding layer properties on the static electromechanical behaviour of a sensor/actuator system. The simulation part is done in this thesis, and future studies in the following areas are suggested:

(1) Corresponding experimental work needs to be conducted to verify the simulation results obtained by using the current sensor/actuator model. Proper modification of the sensor/actuator model may be needed according to experiment results.

(2) In the next step, cracks with different sizes and orientations should be introduced into the host medium. The wave reflected by the cracks should be collected by piezoelectric sensors and identification of cracks should be conducted, both theoretically and experimentally.

(3) The current two dimensional model can be further extend into a 3-D model in order to provide more accurate simulation results for the real sensor/actuator system, which, in reality, is always three dimensional.

(4) Besides, simulation and experiments need to be conducted for different selections of existing adhesives, sensor/actuator and host medium materials in order to give more concrete suggestions about the optimal design of sensor/actuator systems.

Bibliography

[1] Gandhi, M.V., Thompson, B.S, 1992. Smart Materials and Structures, Chapman Hall, London.

[2] Banks, H.T., Smith, R.C., Wang, Y. 1996. Smart Material Structures: Modelling, Estimation and Control, Masson, John Wiley and Sons, Paris.

[3] Tani, J., Takaga, T., Qiu, J., 1998. Intelligent material systems: Application of functional materials. ASME Appl. Mech. Rev. 51, 505-521.

[4] Boller, C. 2000. Next generation structural health monitoring and its integration into aircraft design. Int. J. Syst. Sci. 31, 1333-1349.

[5] Denoyer, K.K., Kwak, M.K., 1996. Dynamic modelling and vibration suppression of a slewing structure utilizing piezoelectric sensors and actuators. J. Sound and Vib. 189, 13-31.

[6] Kwak, M.K., Sciulli D., 1996. Puzzy-logic based vibration suppression control experiments on active structures. J. Sound and Vib. 191, 15-28.

[7] Park, J.M., Kim, D.S., Han, S.B., 2000. Properties of interfacial adhesion for vibration controllability of composite materials as smart structures. Comp. Sci. Tech. 60, 1953-1963.

[8] Rabinovitch, O., Vinson, J.R., 2002. Adhesive layer effects in surface-mounted piezoelectric actuators. J. Intell. Mater. Syst. Struct. 13, 689-704.

[9] Crawley, E.F., de Luis, J., 1987. Use of piezoelectric actuators as elements of intelligent structures. AIAA J. 25, 1373-1385.

[10] Crawley, E.F., Anderson, E.H., 1990. Detailed models of piezoelectric actuation of beams. J. Intell. Mater. Syst. Struct. 1, 4-25.

[11] Lin, M.W., Rogers, C.A., 1993a. Modeling of the actuation mechanism in a beam structure with induced strain actuators. Proceedings of AIAA/ASCE/ASME/ASC 34th Structures, Structural Dynamics and Materials Conference, Part VI, La Jolla, CA, April 19-22, 3608-3617.

[12] Lin, M.W., Rogers, C.A., 1993b. Actuation response of a beam structure with induced strain actuators. ASME Adapt. Struct. Mater. Syst. AD 35, 129-139.

[13] Dimitriadis, E.K., Fuller, C.R., Rogers, C.A., 1991. Piezoelectric actuators for distributed noise and vibration excitation of thin plates. ASME J. Vib. Acoust. 13, 100-107.

[14] Tzou, H.S., Tseng, C.I., 1991. Distributed vibration control and identification of coupled elastic/piezoelectric systems. Mech. Syst. Signal Proces. 5, 215-231.

[15] Wang, B.-T., Rogers, C.A., 1991. Laminate plate theory for spatially distributed induced strain actuators. J. Comp. Mater. 25, 433-452.

[16] Tauchert, T.R., 1992. Piezothermoelastic behavior of a laminated plate. J. Therm. Stress. 15, 25-37.

[17] Mitchell, J.A., Reddy, J.N., 1995. A study of embedded piezoelectric layers in composite cylinders. ASME J. Appl. Mech. 62, 166-173.

[18] Han, J.-H., Lee, I., 1998. Analysis of composite plates with piezoelectric actuators for vibration control using layerwise displacement theory. Comp. Part B 29, 519-672.

[19] Reddy, J.N., 1999. On laminated composite plates with integrated sensors and actuators. Eng. Struct. 21, 568-593.

[20] Wang, X.D., Meguid, S.A., 2000. On the electroelastic behaviour of a thin piezoelectric actuator attached to an infinite host structure, Int. J. Solids Struct. 37, 3231-3252.

[21] Zhang, J.Q., Zhang, B.N., Fan, J.H., 2003a. A coupled electromechanical analysis of a piezoelectric layer bonded to an elastic substrate: Part I. Development of governing equations. Int. J. Solids Struct. 40, 6781-6797.

[22] Zhang, B.N., Zhang, J.Q., Fan, J.H., 2003b. A coupled electromechanical analysis of a piezoelectric layer bonded to an elastic substrate: Part II. Numerical solution and applications. Int. J. Solids Struct. 40, 6612-6799.

[23] Seeley, C.E., Chattopadhyay, A., 1996. Modeling delaminations in smart composite laminates. Proceedings of the 37th AIAA/ASME/ASCE/AHS/ASC Structures, Structural Dynamics and Materials Conference, Salt Lake City, UT, April 18-19, 109-119.

[24] Seeley, C.E., Chattopadhyay, A., 1998. Experimental investigation of composite beams with piezoelectric actuation and debonding. Smart Mater. Struct. 7, 502-511.

[25] Tylikowski, A., 2001. Effects of piezoactuator delamination on the transfer functions of vibration control systems. Int. J. Solids Struct. 38, 2189-2202.

[26] Tong, L., Sun, D.C., Atluri, S.N., 2001. Sensing and actuating behaviors of piezoelectric layers with debonding in smart beams. Smart Mater. Struct. 10, 713-723.

[27] Sun, D.C., Tong, L., Atluri, S.N., 2001. Effects of piezoelectric sensor/actuator debonding on vibration control of smart beams. Int. J. Solids Struct. 38, 9033-9051.

[28] Luo, Q.T., Tong, L.Y., 2002. Exact static solutions to piezoelectric smart beams including peel stresses. II. Numerical results, comparison and discussion, Int. J. Solids Struct. 39, 4697-4722.

[29] Sun, D.C., Tong, L., 2003. Closed-loop based detection of debonding of piezoelectric actuator patches in controlled beams. Int. J. Solids Struct. 40, 2449-2471.

[30] Bhalla, S., Soh, C.K., 2004. Electromechanical impedance modelling for adhesively bonded piezo-transducers. J. Intell. Mater. Syst. Struct. 15, 955-72.

[31] Della, C.N., Shu, D., 2007. Vibration of delaminated composite laminates: A review. ASME Appl. Mech. Rev. 60, 1-20.

[32] Tressler, J.F., ALkoy, S., Newnham, R.E., 1998. Piezoelectric sensors and sensor materials. J. Electroceramics 2, 257-272.

[33] Berlincourt, D., 1992. Piezoelectric ceramic compositional development. J. Acoust. Soc. Am. 91, 3034-3040.

[34] Jaffe, B., Cook, W.R., Jaffe, J., 1971. Piezoelectric Ceramics, Academic Press, New York.

[35] Ikeda, T., 1990. Fundamentals of Piezoelectricity, Oxford University Press, New York.

[36] Pohanka, R.C., Smith, P.L., 1988. Electronic Ceramics, Properties, Devices and Applications, (edited by L. N. Levinson), Chapter 2, Marcel Dekker, New York.

[37] Banks, H.T., Emeric, P.R., 1998. Detection of non-symmetrical damage in smart plate-like structures. Journal of Intelligent Material Systems and Structures 9, 818-828.

[38] Valdes, S.H.D., Soutis, C., 1999. Application of the rapid frequency sweep technique for delamination detection in composite laminates. Advanced Composites Letters 8, 19-23.

[39] Chattopadhyay, A., Nam, C., Kim, Y., 2000. Damage detection and vibration control of a delaminated smart composite plate. Advanced Composites Letters 9, 7-15.

[40] Winston, H.A., Sun, F., Annigeri, B.S., 2001. Structural health monitoring with piezoelectric active sensors. Journal of Engineering for Gas Turbines and Power, 123, 353-358.

[41] Giurgiutiu, V., Zagrai, A.N., 2002. Embedded self-sensing piezoelectric active sensors for on-line structural identification. J. Vib. Acoust. 124, 116-125.

[42] Inman, D.J., Dosch, J.J., Garcia, E., 1992. A self-sensing piezoelectric actuator for collocated control. Journal of Intelligent Materials and Smart Structures 3, 166-185.

[43] Chen, L.-W., Lin, C.-Y., Wang, C.-C., 2002. Dynamic stability analysis and control of a composite beam with piezoelectric layers. Comp. Struct. 56, 97-109.

[44] Mukherjee, A., Saha Chaudhuri, A., 2002. Active control of dynamic instability of piezolaminated imperfect columns. Smart Mater. Struct. 11, 874-879.

[45] Thompson, S.P., Loughlan, J., 1995. The active buckling control of some composite column strips using piezoceramic actuators. Comp. Struct. 32, 59-67.

[46] Chase, J.G., Yim, J., 1999. Optimal stabilization of column buckling. ASCE J. Eng. Mech. 125, 987-993.

[47] De Faria, A.R., De Almedia, S.F.M., 1999. Enhancement of pre-buckling behavior of composite beams with geometric imperfections using piezoelectric actuators. Comp. B 30, 43-50.

[48] Wang, Q., 2002. On buckling of column structures with a pair of piezoelectric layers. Eng. Struct. 24, 199-205.

[49] Wang, Q., Varadan, V.K., 2003. Transition of the buckling load of beams by the use of piezoelectric layers. Smart Mater. Struct. 12, 696-702.

[50] Yang, Y., Ju, C., Soh, C.K., 2003. Analytical and semi-analytical solutions for vibration control of a cantilevered column using a piezoelectric actuator. Smart Mater. Struct. 12, 193-203.

[51] Sloss, J.M., Brucha, J.C., Sadekc, I.S., Adalid, S., 2003. Piezo patch sensor/actuator control of the vibrations of a cantilever under axial load. Comp. Struct. 64, 423-428.

[52] Pan, J., 1994. Further studies of the dynamic response of a simply supported beam excited by a pair of out-of-phase piezoelectric actuators. Journal of Intelligent Material Systems and Structures 5, 654-664.

[53] Shen, I.Y., 1995. Bending and torsional vibration control of composite beams through intelligent constrained-layer damping treatments. Smart Mater. Struct. 4, 340-355.

[54] Shen, I.Y., 1994. Bending-vibration control of composite and isotropic plates through intelligent constrained-layer treatments. Smart Mater. Struct. 3, 59-70.

[55] Yang, B., Tan, C.A., 1992. Transfer functions of one-dimensional distributed parameter systems. J. Appl. Mech. 59, 1009-1014.

[56] Koconis, D.B., Kollar, L.P., Springer, G.S., 1994. Shape control of composite plates and shells with embedded actuators I. Voltages specified. J. Compos. Mater. 28, 415-458.

[57] Koconis, D.B., Kollar, L.P., Springer, G.S., 1994. Shape control of composite plates and shells with embedded actuators II. Desired shape specified. J. Compos. Mater. 28, 459-483.

[58] Chandrashekhara, K., Varadarajan, S., 1997. Adaptive shape control of composite beams with piezoelectric actuators. J. Intell. Mater. Syst. Struct. 8, 112-124.

[59] Fitzpatrick, B.G., 1997. Shape matching with smart material structures using piezoceramic actuators. J. Intell. Mater. Syst. Struct. 8, 876-882.

[60] Banks, H.T., Ito, K., Wang, Y., 1993. Computational methods for identifications and feedback control in structures with piezoceramic actuators and sensors. J. Intell. Mater. Syst. Struct. 4, 469-476.

[61] Irschik, H., Adam, C., Heuer, R., Ziegler, F., 1998. An Exact Solution for Static Shape Control using Piezoelectric Actuation Adaptive Structures, ASME Publication 15, 103-113.

[62] Wang, C.M., Ang, K.K., Ajit, A., 2000. Shape control of laminated cantilevered beams with piezoelectric actuators. J. Intell. Mater. Syst. Struct. 10, 164-175.

[63] Achuthan, A., Keng, A.K., Ming, W.C., 2001. Shape control of coupled nonlinear piezoelectric beams. Smart Mater. Struct. 10, 914-924.

[64] Liang, C., Sun, F.P., Rogers, C.A., 1994. Coupled electro-mechanical analysis of adaptive material system-determination of the actuator power consumption and energy transfer. Journal of Intelligent Material Systems and Structures 5, 12-20.

[65] Sun, F.P., Chaudhry, Z., Rogers, C.A., Majmundar, M., Liang, C., 1995. Automated real-time structure health monitoring via signature pattern recognition. Proceedings of the SPIE Conference on Smart Structures and Materials 2443, 236-247.

[66] Chaudhry, Z., Sun, F.P., Rogers, C.A., 1994. Health monitoring of space structures using impedance measurements. Fifth International Conference on Adaptive Structures, Sendai, Japan, Dec. 5-7.

[67] Chaudhry, Z., Joseph, T., Sun, F., Rogers, C., 1995. Local-area health monitoring of aircraft via piezoelectric actuator/sensor patches. Proceedings, SPIE North American Conference on Smart Structures and Materials 2443, San Diego.

[68] Giurgiutiu, V., Rogers, C.A., 1997. Electromechanical (E/M) impedance method for structural health monitoring an non-destructive evaluation. Int. Workshop on Structural Health Monitoring, Stanford University, CA, Sept. 18-20.

[69] Quinn, P., Palacios, L., Carman, G., Speyer, J., 1999. Health monitoring of structures using directional piezoelectrics. 1999 ASME Mechanics and Materials Conference, Blacksburg, VA, Jun. 27-30.

[70] Lopes V. Jr., Park, G., Cudney, H., Inman, D., 1999. Smart structures health monitoring using artificial neural network. 2nd International Workshop of Structural Health Monitoring, Stanford University, Sept. 8-10.

[71] Chang, F.K., 1995. Built-in damage diagnostics for composite structures. Proceedings of the 10th International Conference on Composite Structures (ICCM-10) 5, 283-289.

[72] Lin, X., Yuan, F.G., 2000. Pre-stack reverse time migration in structural health monitoring. 41st AIAA/ASME/ASCE/AHS/ASc Structures, Structural Dynamics and Materials Conference and Exhibit, Atlanta, 1984-1994.

[73] Park, J.M., Kong, J.W., Kim, D.S., Yoon, D.J., 2005. Nondestructive damage detection and interfacial evaluation of single-fibers/epoxy composites using PZT, PVDF and P(VDF-TrFE) copolymer sensors. Composites Science and Technology 65, 241-256.

[74] Farrar, C.R., Doebling, S.W., Nix, D.A., 2001. Vibration-based structural damage identification. Philosophical Transactions: Mathematical, Physical and Engineering Sciences 359, 131-149.

[75] Biemans, C., Staszewski, W.J., Boller, C., Tomlinson, G.R., 1999. Crack detection in metallic structures using piezoceramic sensors. Damage Assessment of Structures Key Engineering Materials 167, 112-121.

[76] Giurgiutiu, V., Zagrai, A., Bao, J.J., 2002. Piezoelectric wafer embedded active sensors for aging aircraft structural health monitoring. Structural Health Monitoring 1, 41-61.

[77] Alleyne, D.N., Cawley, P., 1992. Optimization of Lamb wave inspection techniques. NDT and E International 25, 11-22.

[78] Wang, B.L., Mai, Y.W., 2002. Fracture of a piezoelectric material layer bonded by two elastic layers. International Journal of Engineering Science 40, 1697-1727.

[79] Akella, P., Chen, X., Cheng, W., Hughes, D., Wen, J.T., 1994. Modelling and control of smart structures with bonded piezoelectric sensors and actuators. Smart Mater. Struct. 3, 344-353.

[80] Nakra, B.C., 2005. Vibration control in machines and structures using viscoelastic damping. J. Sound Vib. 211, 449-465.

[81] Pietrzakowski, M., 2001. Active damping of beams by piezoelectric system: effects of bonding layer properties. Solids Struct. 38, 7885-7897.

[82] Frostig, Y., 1998. Buckling of sandwich panels with a transversely flexible core: High-order theory. Int. J. Solids Struct. 35, 183-204.

[83] Frostig, Y., Rabinovitch, O., 2000. Behavior of sandwich panels with multi-skin construction or a multi-layered core: A high-order approach. Journal of Sandwich Structures and Materials 2, 181-213.

[84] De Faria, A.R., 2003. The impact of finite stiffness bonding on the sensing effectiveness of piezoelectric patches. Smart Mater. Struct. 12, N5-N8.

[85] Han, L., Wang, X.D., Sun, Y., 2008. The effect of bonding layer properties on the dynamic behaviour of surface-bonded piezoelectric sensors. Int. J. Solids Struct. 45, 5599-5612.

[86] Han, L., Wang, X.D., Zuo, M., 2008. The dynamic behavior of a surface-bonded piezoelectric actuator with a bonding layer. Acta Mech. DOI: 10.1007/s00707-008-0098-3.

[87] Muskhelishvili, N.I., 1953. Some Basic Problems of the Mathematical Theory of Elasticity, Noordhoff, Groningen.

[88] Park, Y.E. 1990. Crack extension force in a piezoelectric material, ASME J. Appl. Mech. 57, 647-653.

[89] Wang, X.D., Huang, G.L. 2006. The coupled dynamic behaviour of piezoelectric sensors bonded to elastic media. J. Intell. Mater. Syst. Struct. 17, 883-894.

[90] Lee, C.K., Moon, F.C., 1989. Laminated piezopolymer plates for torsion and bending sensors and actuators. J. Acoust. Soc. Am. 85, 2432-2439.